The Pennsylvania State University

The Graduate School

Department of Electrical Engineering

THERMAL SENSING USING MICROMACHINED Y-CUT QUARTZ RESONATORS

A Thesis in

Electrical Engineering

by

Ashish Patwardhan

Submitted in Partial Fulfillment
of the Requirements
for the Degree of

Master of Science

August 2008

The thesis of Ashish Patwardhan was reviewed and approved* by the following:

Srinivas Tadigadapa
Associate Professor of Electrical Engineering
Thesis Advisor

Jerzy Ruzyllo
Professor of Electrical Engineering
Professor of Material Science and Engineering

W. Kenneth Jenkins
Professor of Electrical Engineering
Head of the Department of Electrical Engineering

*Signatures are on file in the Graduate School

ABSTRACT

In this thesis, a process for the fabrication of miniature Y-cut Quartz resonators is presented. The fabricated Y-cut resonators were characterized and their resonance characteristics were compared to theory.

Y-cut quartz resonators are temperature sensitive (90ppm/^{o}C).This property of these resonators enables us to use these sensors as a thermal sensor. This sensor is ideal to monitor small quantities of heat generated as in enzymatic reactions or as an Infrared sensor. A method for the measurement of infrared radiation using the Y-cut resonators is presented in this thesis.

A circuit is proposed for the real time frequency monitoring of the resonator. This circuit will be able to record the smallest change in frequency in real time, thus aiding in the analysis of the process under study.

TABLE OF CONTENTS

LIST OF FIGURES

LIST OF TABLES

ACKNOWLEDGEMENTS

I would like to thank Dr. Srinivas Tadigadapa for mentoring me and guiding me during my Masters Research.

I would also like to thank my lab mates, Prasoon Joshi, Nicholas Duarte, Ping Kao, Andrew Hirsh, Kiron Mateti, and Han Guen Yu for all their help and support during the course of my research and for making the whole experience of research very enjoyable.

I would also like to thank Dave Sarge and Fawn Houtz for their unconditional support in the clean room.

I would also like to acknowledge support from my family and friends without whose encouragement and love this would not have been possible.

Chapter 1

Introduction

This Chapter will introduce the quartz resonator. The various properties of quartz resonators are discussed. The advantages of miniaturization of quartz resonators and its applications are presented.

Quartz resonators, popularly known as, quartz crystal microbalance –QCM is a well known high performance mass sensing device. A QCM measures mass per unit area via a linearly proportional shift in resonance frequency of a quartz crystal resonator and is given by the now famous Sauerbrey equation [8] as:

$$\Delta f = - S_c \frac{\Delta m}{A} \qquad \textbf{1.1}$$

where, A is the area of the overlapping electrodes of the QCM, Δf is the change in the resonance frequency of the resonator with deposition of mass on one of its electrode, S_c is the Sauerbrey constant and Δm is the change in the mass on the electrode of the QCM. The negative sign in the above equation indicates that the resonance frequency decreases as mass is added on the electrodes of the QCM.

The resonance frequency is shifted by the addition or removal of a small mass due to oxide removal or film deposition at the surface of the acoustic resonator. The QCM

can be used under vacuum, in gas phase ("gas sensor", first use described by [1]) and more recently in liquid environments.

In the manufacture of quartz resonators, plates are cut from a quartz crystal along precisely controlled directions with respect to the crystallographic axes. These various "cuts" of quartz have different properties. The Y-cut quartz is sensitive to temperature and its frequency is dependent on the temperature. It is thus possible to use such cuts of quartz as a temperature sensor [13]. This thesis will focus on the use of such temperature sensitive quartz resonators for thermal sensing applications.

1.1 Piezoelectric Effect

Piezoelectricity is the ability of some materials (notably crystals and certain ceramics) to generate an electric potential [2] in response to applied mechanical stress. This takes place in the form of separation of electric charge across the crystal lattice. If the material is not short-circuited, the developed charge induces a voltage across the material. The word is derived from the Greek *piezein*, which means to squeeze or press.

The piezoelectric effect is reversible in that materials exhibiting the *direct piezoelectric effect* (the production of electricity when stress is applied) also exhibit the *converse piezoelectric effect* (the production of stress and/or strain when an electric field is applied). For example, lead zirconate titanate (PZT) crystals exhibit a maximum shape change of about 0.1% of the original dimension.

The piezoelectric effect has found applications in high voltage applications, sensors, actuators, frequency standards, motors, etc., and the relationship between applied voltage and mechanical deformation is well known; this allows probing an acoustic resonance by electrical means.

1.2 Quartz Crystal

Quartz is the most abundant mineral in the earth's crust. It is made up of a lattice of silica (SiO_2). It belongs to the rhombohedral crystal system. The ideal crystal shape is a six-sided prism (As shown in Fig 1.1 [4]) terminating with six-sided pyramids at each end. The prism faces are called as *m*-faces and the pyramid faces are designated as *R*- and *r*-faces. The *R*-faces are called as major rhomb faces and the *r*-faces are called as minor rhomb faces.

In nature quartz crystals are often twinned, distorted, or so intergrown with adjacent crystals of quartz or other minerals as to only show part of this shape, or to lack obvious crystal faces altogether and appear massive. Due to natural quartz being so often twinned, much of the quartz used in industry is synthesized. Large, flawless and untwinned crystals are produced in an autoclave via the hydrothermal process. Figure 1.1 [4] also depicts the various quartz crystal cuts with respect to the crystal orientation. The principle or the z-axis in the quartz is the axis of three fold symmetry in quartz. This

means that all the physical properties repeat each 120° as the crystal is rotated about the Z-axis.

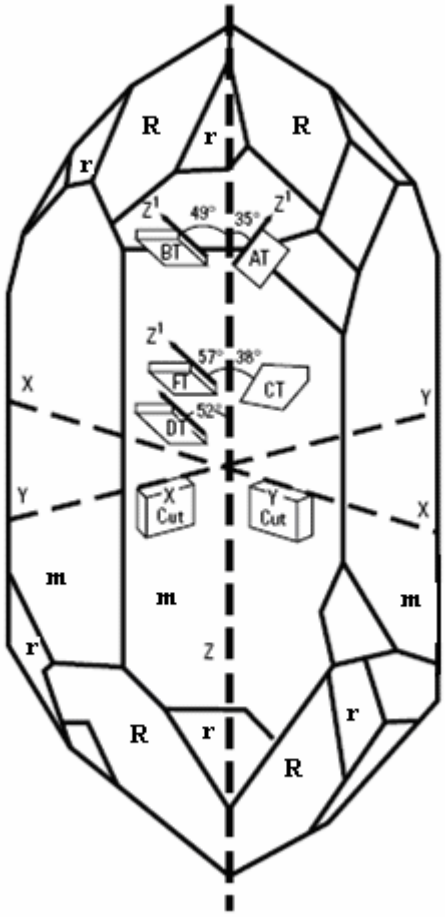

Figure **1-1**:**:** *Schematic depiction of a grown quartz crystal. Also shown is the crystallographic orientation for the AT and Y cut along with other cuts. AT-cut is the most popular cut of quartz crystal in use [4].*

Quartz's piezoelectric properties were discovered by Jacques and Pierre Curie in 1880 [3]. With the application of stress, there is a potential developed in the crystal. There is a

net dipole in the Quartz crystal due to the non linear Si-O bonds. Applying an electric field causes the realignment of the opposite ends of the dipole (in the direction of the applied electric field). An alternating current between the electrodes of a properly cut crystal, causes the dipole displacement to vary with the electric field and a standing shear wave can be generated. The frequency of these vibrations is approximately equal to the frequency of the applied alternating field.

The quartz oscillator or resonator was first developed by Walter Guyton Cady in 1921. George Washington Pierce designed and patented quartz crystal oscillators in 1923. Warren Marrison created the first quartz oscillator clock based on the work of Cady and Pierce in 1927 [3].

The Q factor which is the ratio of frequency and bandwidth, can be as high as 10^6. Such a narrow resonance leads to highly stable oscillators and a high accuracy in the determination of the resonance frequency. The quartz resonator sensor exploits this ease and precision for sensing. Commercially available QCM's have a resolution down to 0.1 Hz on crystals with a fundamental resonant frequency of about 5 MHz.

1.3 Vibration Modes

The quartz plate, like all plates, has many modes of vibration. There are three basic modes of vibration as illustrated in *Figure* **1-2**

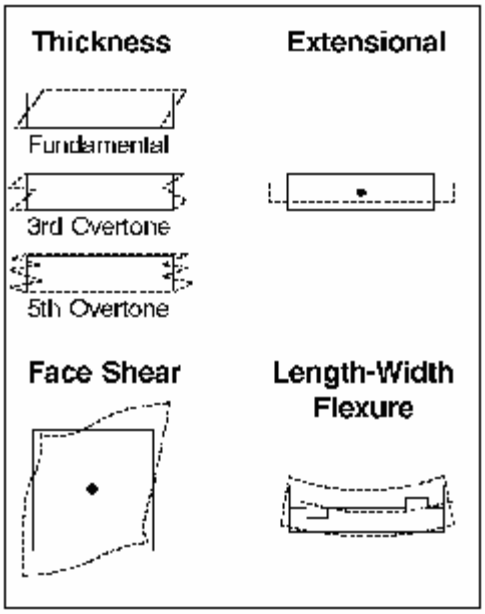

Figure 1-2: *Various Modes of operation of Quartz* [16]

(a) Flexure mode (bending or bowing); Cuts: 5° X, NT; Frequency ~ 100 kHz.

(b) Extensional Mode (displacement along the length of the plate); Cuts: MT, GT; Frequency: 40 – 200 kHz.

(c) Shear Mode (sliding two parallel planes in opposite directions). This mode is subdivided into:

Face Shear; Cuts: CT, DT; Frequency: 100 – 600 kHz.

Thickness Shear; Cuts: AT, BT, SC and the Y-cut

Properly oriented electrodes excite the desired mode of vibration. Although a large number of different cuts have been developed, some are used only at low frequency; while others are used in applications other than frequency control. Except for the low-frequency tuning fork resonators used in quartz watches and clocks, almost all quartz resonators in today's applications use a thickness-shear mode. At frequencies above approximately 1 MHz, AT-cut and SC-cut are primarily used.

1.4 Frequency response of a Quartz Crystal

The fundamental frequency of a quartz resonator can be given by Eq. **1.2**

$$f_o = \frac{v}{2d} = \frac{1}{2d}\sqrt{\frac{c_{ij}}{\rho}} \qquad \textbf{1.2}$$

Where, f_o is the fundamental resonance frequency of the quartz plate, d is the thicknes, ρ is the density of the quartz crystal (2.648 g cm-3) ,c_{ij} is the elastic modulus (the ratio of the stress and strain) associated with the elastic wave propagated in quartz and v is the velocity with which an elastic wave propagates in the quartz.

All the terms used in the above equation are temperature dependent. Also, the temperature coefficients of the elastic modulus (c_{ij}) are dependent on the specific cut of quartz used. One of the reasons that quartz resonators are useful for frequency control

and gravimetric applications is that, at certain angles of cut – such as the AT cut, the temperature coefficients of c_{ij} cancels the temperature coefficients of the other terms in Eq. **1.2**, i.e., angles of cut exist in quartz that can provide zero temperature coefficient of frequency within a certain range. At other angles of cut, it is possible to obtain steep and monotonic frequency versus temperature characteristics that can be useful for thermometers and other thermal sensing applications.

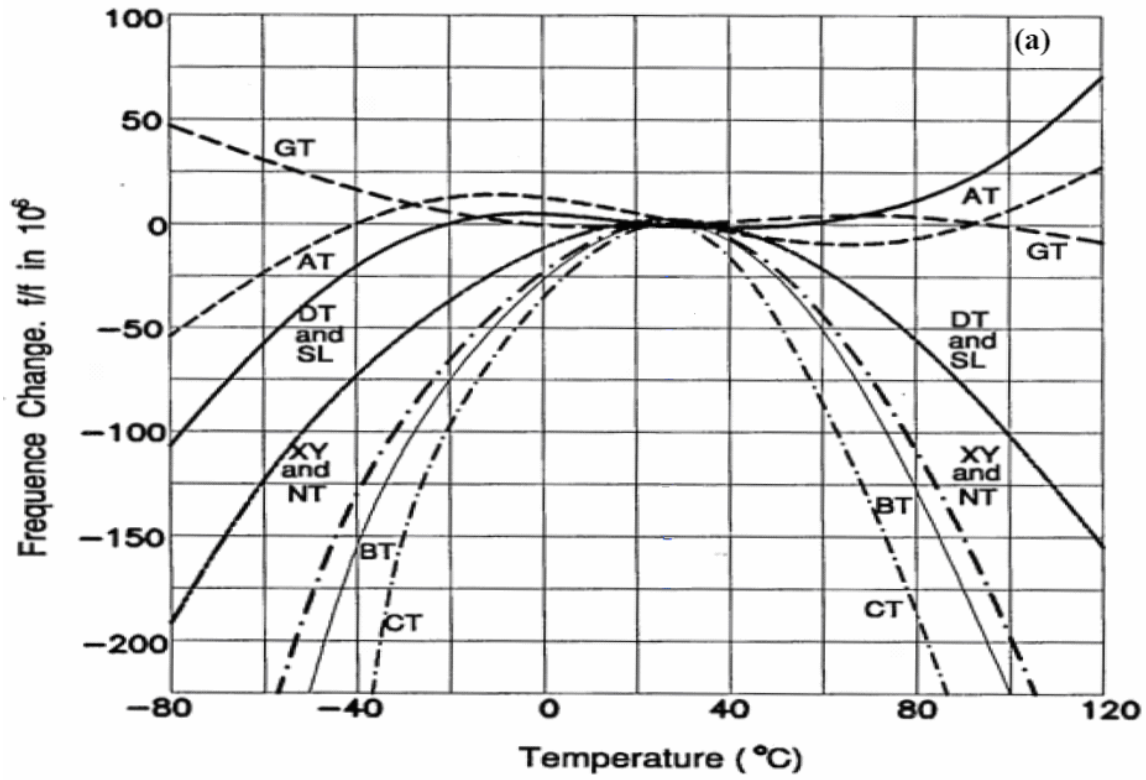

Figure **1-3**: *Variation in resonance frequency of quartz resonator for different cuts.[**6**]*

As can be seen from Figure **1-3** the minimum variation in frequency with temperature at ambient room temperature is exhibited by AT and GT cuts. The main reason for the

prolific use of AT-cut quartz crystal is their exceptional frequency stability, and high quality (*Q*-) factor. The material properties of single-crystal AT-cut quartz are extremely stable with time, temperature, and other environmental changes, as well as highly repeatable from one specimen to another. This enables us to use the AT cut quartz as a gravimetric sensor.

The quartz resonator frequency can monotonically vary with temperature with a slope of about $10^{-4}/^{o}C$. The Y-cut quartz which we shall use in this thesis as a sensor has a temperature sensitivity of about 90ppm/^{o}C. We shall exploit this ability of quartz to make a temperature sensor.

1.5 Equivalent Circuit of a Quartz Resonator

1.5.1 The Mason Model:

A general one dimensional model for the electrical characterization of a quartz resonator (piezoelectric plate) can be given by the Mason model as shown in Figure **1-4** . This circuit is named after Warren Mason who did pioneering work in crystal acoustics.

The transformer represents the conversion of electrical energy to acoustic energy in the quartz resonator. An excellent derivation of the Mason model is given by Rosenbaum [**10**].

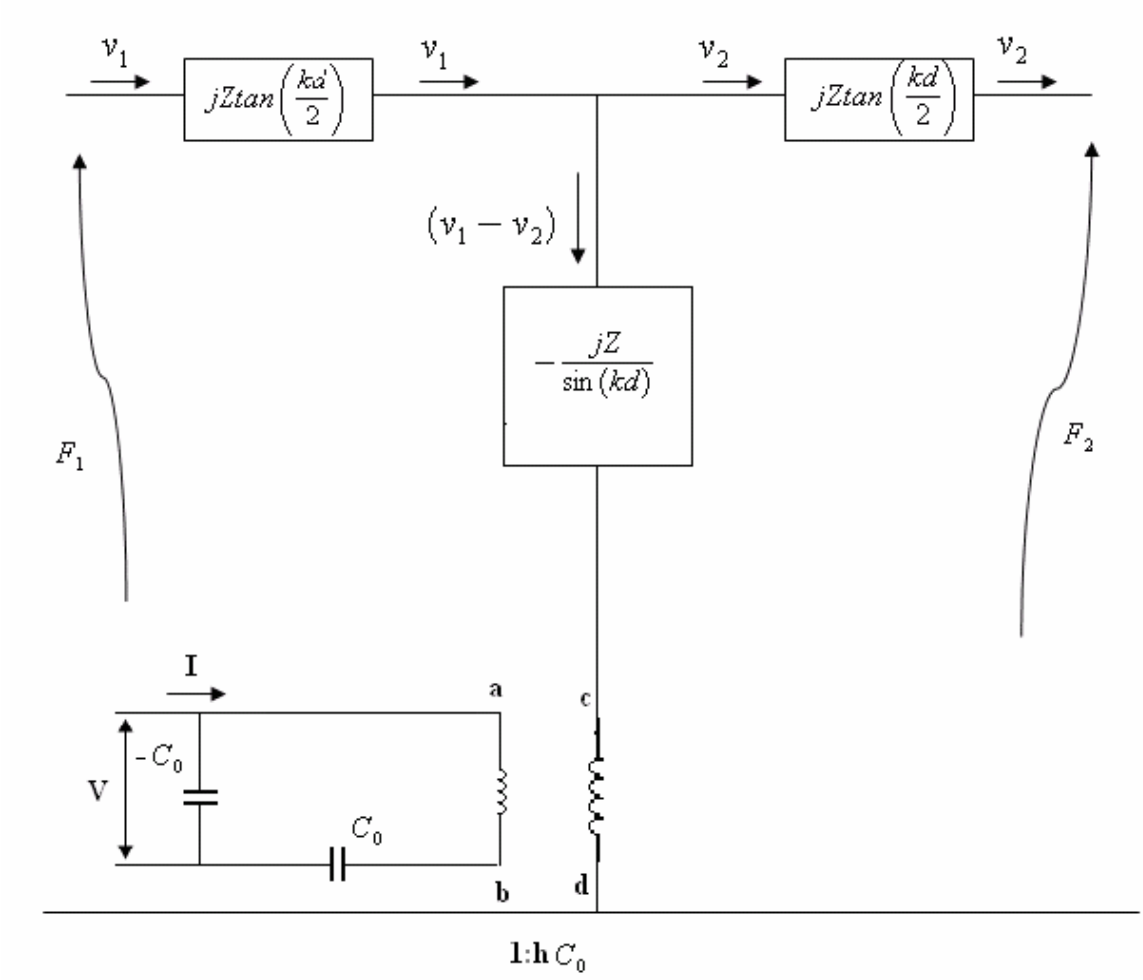

Figure 1-4: Final form of the three-port Mason model equivalent circuit

1.5.2 The Butterworth-Van Dyke Equivalent Model:

The Mason model equations [10] for the piezoelectric slab can be written as

$$0 = Z_T\left(\frac{v_1}{jtan\,(kd)} - \frac{v_2}{jsin\,(kd)}\right) + \frac{h}{j\omega} I \qquad \textbf{1.3}$$

$$-Z_s v_2 = Z_T\left(\frac{v_1}{jsin\,(kd)} - \frac{v_2}{jtan\,(kd)}\right) + \frac{h}{j\omega} I \qquad \textbf{1.4}$$

$$V = \frac{h}{j\omega}(v_1 - v_2) + \frac{I}{j\omega C_0} \qquad \textbf{1.5}$$

We can see that the current I is an independent variable (since the electric field is composed of external and acoustically generated components) In a resonator, the piezoelectric layer is bounded by an acoustic short (air)hence $Z_s = 0$.

Eq. **1.4** can then be written as

$$0 = Z_T\left(\frac{v_1}{jsin\,(kd)} - \frac{v_2}{jtan\,(kd)}\right) + \frac{h}{j\omega} I \qquad \textbf{1.6}$$

Solving equations **1.4** and **1.6** , we get

$$\frac{v_1}{I} = -\frac{\frac{h}{j\omega}}{\frac{Z}{jtan\,(kd)} + \frac{Z}{jsin\,(kd)}} \qquad \textbf{1.7}$$

Solving the equations for the input impedance $V/I = Z_{in}$, we get

$$
\begin{aligned}
Z_{in} &= \frac{V}{I} = \frac{h}{j\omega}\cdot\frac{v_1 - v_2}{I} + \frac{1}{j\omega C_0} \\
&= \frac{-2h^2}{j\omega^2 Z}\left(\frac{1}{\frac{1}{\tan(kd)} + \frac{1}{\sin(kd)}}\right) + \frac{1}{j\omega C_0} \\
&= \frac{1}{j\omega C_0}\left(1 - \frac{2C_0 h^2}{\omega Z}\tan\left(\frac{kd}{2}\right)\right) \qquad \textbf{1.8} \\
&= \frac{1}{j\omega C_0}\left(1 - k_t^2 \frac{\tan\left(\frac{kd}{2}\right)}{\frac{kd}{2}}\right)
\end{aligned}
$$

From Eq. **1.8** we can show that the resonator can be represented by a constant clamped capacitance in parallel with an acoustic or a motional arm- which can be capacitive or inductive. This circuit as shown in is the Butterworth-Van Dyke circuit.

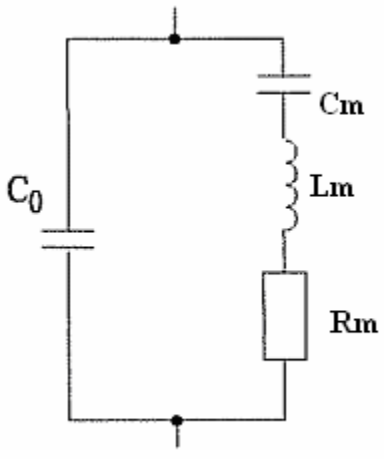

Figure **1-5**: Butterworth-Van Dyke equivalent circuit for a resonator

For the fundamental mode, the input admittance can be given as

$$Y_{in} = j\omega C_0 + \frac{1}{j\left(\omega L_m - \frac{1}{\omega C_m}\right)} = \frac{-\left(\omega L_m - \frac{1}{\omega C_m}\right)\omega C_o + 1}{j\left(\omega L_m - \frac{1}{\omega C_m}\right)} \quad \textbf{1.9}$$

The input impedance is

$$Z_{in} = Y_{in}^{-1} = j\frac{\omega L_m - \frac{1}{\omega C_m}}{1 - \omega^2 C_0 L_m + \frac{C_0}{C_m}} \quad \textbf{1.10}$$

At series resonance, the impedance is zero, hence

$$\omega_r = \frac{1}{\sqrt{L_m C_m}} \quad \textbf{1.11}$$

At parallel resonance, the impedance is infinite (assuming no resistance)

$$\omega_p = \sqrt{\frac{C_m + C_0}{L_m C_o C_m}} = \frac{1}{\omega_r}\sqrt{\frac{C_m + C_0}{C_0}} \quad \textbf{1.12}$$

We can also relate the electromechanical coupling factor as shown in Eq. **1.13**

$$\frac{C_m}{C_0} = \frac{8\,k_T^2}{N^2\,\pi^2} \tag{1.13}$$

The motional resistance can be represented as:

$$R_m = \frac{\pi\,\eta\varepsilon_r\,\varepsilon_0}{8\,k_t^2\,\rho A\omega v_a} \tag{1.14}$$

Where, A is the electrode area and ω is the operating frequency, and η is the viscosity. The values of C_m and L_m can be calculated from fundamental acoustic and electrical parameters (and Eq. **1.11**) as

$$C_m = \frac{8}{\pi^2}\,k_t^2\,C_0 \tag{1.15}$$

$$L_m = \frac{\pi^3\,v_a}{8\omega_r^3\,\varepsilon_r\,\varepsilon_0\,Ak_t^2} \tag{1.16}$$

The quality factor of the resonator can be calculated as

$$Q = \frac{Energy\ stored}{Energy\ dissipated\ per\ cycle} = \frac{\omega_r\,L_m}{R_m} = \frac{v_a^2\,\rho}{\omega_r\,\eta} \tag{1.17}$$

1.6 Resonance Frequencies

The electrical response of a quartz resonator can be obtained from the lumped parameter Butterworth Van-Dyke model as described in the previous section and can be shown as in Figure **1-6**

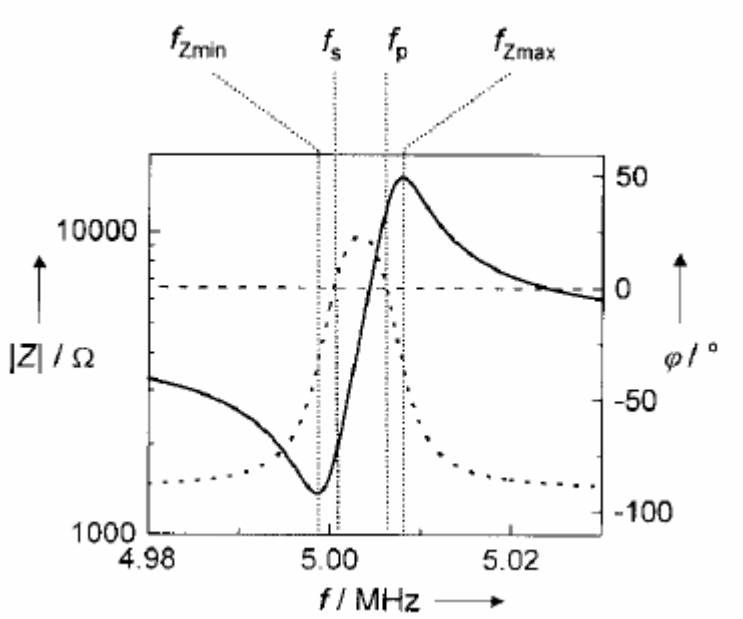

Figure 1-6:Simulated impedance spectrum from the Butterworth Van-Dyke equivalent circuit showing the resonance frequencies. [15]

We can see two resonance frequencies at phase shift φ=0, called the series resonance frequency (f_s) and the parallel resonance frequency (f_p). If the presence of the motional resistance R_m is ignored, these frequencies correspond to the minimum and maximum impedance (Z). With the presence of R_m, the two frequencies are split into f_{Zmin}, the frequency at minimal impedance and f_s, the frequency at zero phase at the lower end of the frequency spectra and correspondingly, f_{Zmax}, the frequency at maximum impedance and f_p, the frequency at zero phase at the higher end of the frequency spectra[15]. The dependence of the resonance frequency on the motional resistance can be given as shown in Table 1-1

Table 1-1: Resonance frequency dependence on motional resistance[15]

f_s	$\frac{1}{2\pi}\sqrt{\frac{1}{L_m C_m}}\left(1+\frac{C_o R_m^2}{2L_m}\right)$
f_{Zmin}	$\frac{1}{2\pi}\sqrt{\frac{1}{L_m C_m}}\left(1-\frac{C_o R_m^2}{2L_m}\right)$
f_p	$\frac{1}{2\pi}\sqrt{\frac{1}{L_m C_m}}\left(1+\frac{C_m}{2C_o}-\frac{C_o R_m^2}{2L_m}\right)$
f_{Zmax}	$\frac{1}{2\pi}\sqrt{\frac{1}{L_m C_m}}\left(1+\frac{C_m}{2C_o}+\frac{C_o R_m^2}{2L_m}\right)$

1.6.1 Admittance and Impedance Circles

The various resonance frequencies can also be plotted from the locus of the admittance or impedance as shown in Figure 1-7 [9]

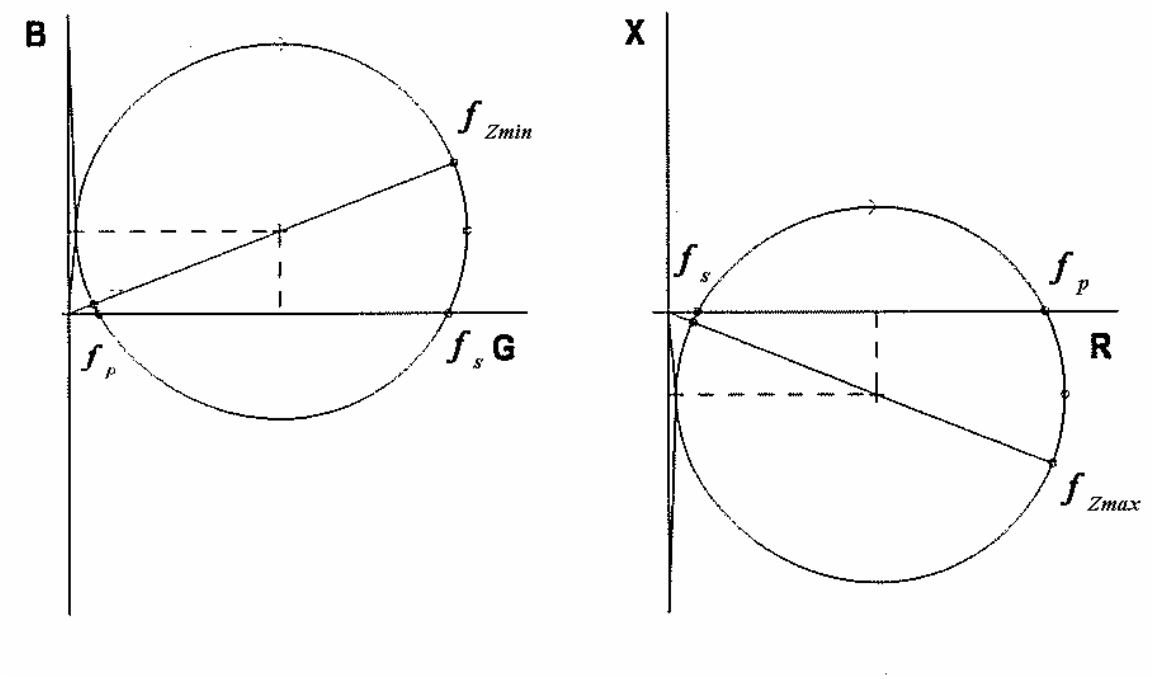

Figure **1-7**: Resonance frequencies for the admittance locus (Y = G +jB) and Impedance locus (Z =R = jX) [**9**]

The Butterworth van-Dyke equivalent model can be used to derive the equation for the electrical admittance(Y) as

$$Y = Y_m + jB_o$$

Where,

$$Y_m = admittance\ of\ the\ motional\ arm = \frac{1}{R_m + jX_m}$$

$$B_o = admittance\ of\ the\ parallel\ arm \quad = \omega C_o$$

Also,

$$X_m = \omega L_m + \frac{1}{\omega C_m}$$

Separating into the real and imaginary parts, we get:

$$Y = \frac{R_m}{R_m^2 + X_m^2} + j \cdot \left(B_o - \frac{X_m}{R_m^2 + X_m^2} \right) \qquad \textbf{1.18}$$
$$= G + j \cdot B$$

The parametric representation can be given as

$$\left(G - \frac{1}{2R_m} \right)^2 + \left(B - B_o \right)^2 = \left(\frac{1}{2R_m} \right)^2 \qquad \textbf{1.19}$$

Using the relation Z = 1/Y , we get the relation for Impedance as

$$Z = \frac{R_m}{\left(R_m B_o \right)^2 + \left(1 - X_m B_o \right)^2} + j \cdot - \frac{R_m^2 B_o - X_m \left(1 - X_m B_o \right)}{\left(R_m B_o \right)^2 + \left(1 - X_m B_o \right)^2} \qquad \textbf{1.20}$$
$$= R + j \cdot X$$

Similarly, the parametric representation can be given as

$$\left(R - \frac{1}{2 R_m B_o} \right)^2 + \left(X + \frac{1}{B_o} \right)^2 = \left(\frac{1}{2R_m B_o} \right)^2 \qquad \textbf{1.21}$$

For a typical quartz resonator the difference in the series resonance frequency and parallel resonance frequency is less than 0.5%. Hence, the parallel susceptance B_o does not change by more than 1% around the resonance frequency values and thus can be replaced by a constant $\overline{B_o} = \omega_s C_o$. Substitution of $\overline{B_o}$ in the parametric equation of the admittance circle gives us a circle with:

$$\text{Centre: } \left[\frac{1}{2R_m}, \overline{B_o} \right] \qquad \textbf{1.22}$$

And

$$\text{Radius: } \frac{1}{2R_m} \text{ .} \qquad \textbf{1.23}$$

The corresponding impedance has

$$\text{Centre: } \left[\frac{1}{2R_m\overline{B_o}^2}, \frac{1}{\overline{\overline{B_o}}}\right] \qquad \textbf{1.24}$$

And

$$\text{Radius: } \frac{1}{2R_m\overline{B_o}^2} \qquad \textbf{1.25}$$

The resonance curves of the manufactured devices will be compared to theory in Chapter 3.

1.7 Spurious Modes

During the operation of a quartz resonator, one often encounters spurious modes. Vibration at frequencies that are not fundamental or overtone (3^{rd}, 5^{th}, 7^{th}, 11^{th} harmonic) modes are referred to as spurious or unwanted modes. The design of the wafer, electrode pattern and amount of metallization can be adjusted to suppress these unwanted modes.

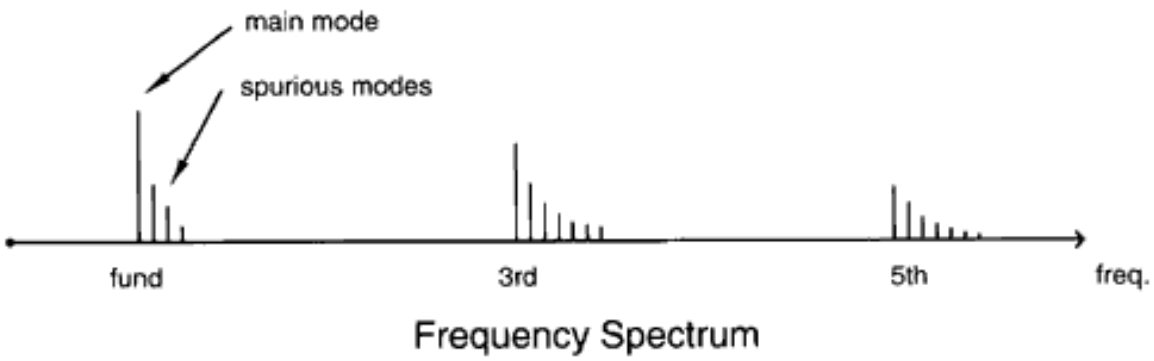

Figure **1-8**: *Spurious modes in a QCM [5]*

Spurious modes can be a problem if the response is as strong as the main mode. When that happens, the oscillator may run on the spurious instead of the main mode. This is called mode hopping.

Fundamental modes of a crystal can achieve the best spurious suppression, while overtone responses are more difficult to control. The spurious modes occur above the main mode within a few hundred kilohertz. The response may look like the plot shown above. In oscillator applications, we can select the strongest mode for operation. Some of the unwanted modes may have steep frequency vs. temperature characteristics. Occasionally, as the temperature changes, at a certain temperature, the frequency of an unwanted mode coincides with the oscillator frequency, which causes so-called “activity dip”. At the activity dip, excitation of the unwanted mode results in extra energy dissipation in the resonator, which results in a decrease in the Q, an increase in the equivalent series resistance, and a change in the frequency of the oscillator. When the resistance increase is sufficiently large, the oscillation may stop, i.e., the oscillator fails.

When the temperature is changed from the activity dip temperature, the oscillation can restart. Unwanted modes can be controlled by proper design and fabrication methods. Maintaining the correct relationships among electrode and resonator plate dimensions (i.e., applying energy trapping rules), and maintaining the parallelism between the major faces of the resonator plate, can minimize the unwanted modes. [5]

1.8 Noise in the quartz resonators

Noise limits the performance of the quartz sensors. It limits the accuracy of the measurement of the resonance frequency and degrades the sensitivity. The main causes for the presence of noise or short term instabilities can be listed as: [17]

1) - Johnson noise caused due to the motional resistance of the resonator and within the oscillator circuitry,
2) Phonon scattering noise in the resonator
3) Changes in external load
4) Thermal response of resonator: (static and dynamic)
5) Temperature fluctuations- an activity dip at the measurement temperature can greatly magnify the frequency fluctuations caused by temperature change
6) Random vibration,
7) Fluctuations in the number of adsorbed molecules.

The standard measure of noise or random fractional frequency fluctuations (also called short-term instabilities) in the time domain is given by the two-sample deviation $\sigma_y(\tau)$

(Allan deviation) [18]. Close to the sensor measurement frequencies, the empirical relationship between the noise floor and the quality factor can be shown as Eq. 1.26

$$\sigma_y(\tau) \geq \frac{1.0 \times 10^{-7}}{Q} \qquad 1.26$$

As the product of the quality factor and the fundamental resonance frequency is a constant for a certain cut of quartz (e.g. $1.6 \times 10^{13}\ Hz$ For AT cut), we can say that the noise floor is directly proportional to the fundamental resonance frequency.

$$\sigma_y(\tau) \propto f_o \qquad 1.27$$

Thus as the fundamental resonance frequency of the quartz resonator increases, correspondingly the noise floor also increases.

The noise due to temperature fluctuation is another contributor to the total noise in the microresonator system, especially for very thin (high frequency) sensors. This noise is due to the quantum nature of heat exchange, i.e. that heat exchange takes place by the absorption and emission of photons and phonons on the surface of the resonator. The smaller the heat capacity (higher the frequency) of a microresonator, the larger the temperature fluctuations due to this noise source. The mean temperature fluctuation, ΔT of any object due to this noise is given by Eq. 1.28

$$\Delta T = \sqrt{\frac{k_B T^2}{C}} \qquad 1.28$$

Where, k_b is the Boltzmann constant and C is the heat capacity, where the heat capacity is given as Eq. **1.29**

$$C = c_v V \qquad \textbf{1.29}$$

Where, $c_v = 2.08 \frac{W \sec}{cm^3 \text{ K}}$ is the specific heat capacity of quartz and 'V' is the volume of the resonator. Thus micromachining causes the heat capacity to decrease, increasing the thermal noise in the system.

However the noise due to thermal variation is much greater than the noise level contributed by the photon fluctuation noise. Realistically speaking, we not reach this limit in the micromachined resonator.

1.9 Need for Miniaturization and Motivation of Work:

The extremely high temperature sensitivity of *Y*-cut quartz of about 10^{-6}°C represents 2-3 orders of magnitude improvement in temperature sensitivity as compared to other temperature dependent phenomena such as Seebeck effect on which a thermopile device is based [**14**]**.** We know that the temperature sensitivity of Y-cut quartz is about 90ppm/°C. [**13**] Miniaturization of the quartz resonators causes an increase in the resonance frequency and a corresponding increase in the Q-factor. This increase in the quality factor of the resonator results in a very stable resonance frequency, reducing the noise caused in the accuracy of its measurement. The increase in the fundamental

resonance frequency of the Y-cut resonator increases the per degree resonance shift obtained in direct proportion as shown in Eq. **1.30**

$$\Delta f = \frac{f_o \times \Delta T}{1000000} \times 90 \qquad \textbf{1.30}$$

where, Δf is the shift in the resonance frequency of the quartz resonator, f_o is the fundamental resonance frequency and ΔT is the change in temperature. As can be seen from the above equation an increase in the fundamental resonance frequency causes an increase in the frequency shift per degree rise in temperature. This makes a resonator with very high resonance frequency capable of resolving and measuring small changes in temperature.

High temperature sensitivity and the low noise performance in quartz resonators is the principle motivation behind their use as temperature or heat sensors. The micromachining of these resonators causes a proportional increase in its resonance frequency. For the temperature sensitive Y-cut samples, the increase in resonance frequency causes a larger shift in frequency with an increase in temperature as explained by Eq. **1.30** . Thus micromachining will allow us to measure small amounts of heat. Reducing the thickness of the resonators also aids in the energy trapping of the acoustic wave within the resonator. This provides a superior isolation resulting in a larger signal and a reduction in the noise. Reduction in the thickness of the resonator membrane reduces its thermal mass and hence a small quantity of heat produces a large change in temperature. Measurement of very small quantities of heat and low noise will make the quartz resonator an effective thermal sensor.

In this thesis, a micromachined quartz resonator and its characteristics are discussed. The use of the resonator as a thermal sensor is presented and its benefits are outlined.

1. W.H. King, Jr., Piezoelectric sorption detector. Analytical Chemistry, 36(9):1735 1739, 1964.

2. NSI-IEEE 176 (1987) Standard on Piezoelectricity

3. http://en.wikipedia.org/wiki/Quartz

4. Virgil, B.E., *Introduction to Quartz Crystal Unit Design*. 1981, Van Nostrand: Reinhold Company.

5. http://www.4timing.com/techcrystal.htm

6. Vig, J.R.; *Tutorial on Quartz Crystals*. 2005

7. http://www.ieee-uffc.org/freqcontrol/quartz/vig/vigstatc.htm

8. Sauerbrey, G., *Verwendung von Schwingquarzen zur Wagung dunner Schichten und zur Mikrowagung.* Z. Phys., 1959. **155**: p. 206-222.

9. Carsten Behling; The non-gravimetric response of thickness shear mode resonators for sensor applications; Shaker Verlag Aachen 1999

10. Joel F Rosenbaum *"Bulk Acoustic Wave Theory and Devices"* Artech, Boston, 1988

11. Bechmann, R., *Quartz at-Type Filter Crystals for Frequency Range 0.7 to 60 Mc.* Proceedings of the Institute of Radio Engineers, 1961. **49**(2)

12. Bechmann, R. 1941: USA Patent No. 2,249,933.

13. Vig, J.R., R.L. Filler, and Y. Kim, "*Uncooled IR imaging array based on quartz microresonators"* Journal of Microelectromechanical Systems, 1996. **5**(2): p. 131-137.

14. Goyal,A, Zhang, Y and Tadigadapa, S "*Y-cut Quartz Resonator based Calorimetric Sensor*" IEEE Sensors 2005.

15. Janshoff, A., H.J. Galla, and C. Steinem, "*Piezoelectric mass-sensing devices as biosensors - An alternative to optical biosensors?"* Angewandte Chemie-International Edition, 2000. **39**(22): p. 4004-4032.

16. Fortiming "*Basic Technology of Quartz Crystal Resonators" A Tutorial.*

17. Vig John R. and Walls Fred L "*A REVIEW OF SENSOR SENSITIVITY AND STABILITY*" 2000 IEEE/EIA International Frequency Control Symposium and Exhibition.

18. IEEE Standard 1139- 1999

Chapter 2

Design and Fabrication of the Quartz Resonators

In this Chapter, the factors taken into consideration for the design of the quartz resonators are discussed. The conclusions drawn to maximize the Q factor and the methods to reduce the spurious modes are stated. The fabrication process is then discussed in a step by step manner to acquaint the user with the various processes involved in the fabrication of these resonators.

2.1: Design of the Quartz Resonators

The design of the resonator has to (i) allow for planned liquid loading experiments on one of the faces of the resonator without the liquid contacting the other electrode, (ii) maintain high resonator characteristics which include maintaining a high Q-factor (i.e. low dissipation) and reducing the spurious modes (unwanted resonance peaks around the fundamental mode).

The peripheral of the resonator has often to be mounted with air or liquid tight seal to form a sample space. The outline of the mount acts as a clamped boundary conditions for the shear mode resonators and therefore a reduction of the displacement at the boundaries is vital to achieve a high Q value. One technique is a trapping of vibration energy in the center portion of QCM. It is realized in the thickness shear mode by making

the resonant frequency of the center portion lower than the resonance frequency of the peripheral area. When the operating frequency is below 10 MHz, the major surfaces of the quartz crystal are usually contoured in either plano-convex, convex-convex or bevel shape [1]. When the operating frequency is much higher, as in our case simple mass loading by electrodes in the center portion on flat surfaces is good enough to cause energy trapping. We are using inverted MESA structures to make an array of sensors for measurement. The inverted mesa configuration offers excellent acoustic isolation from the other pixels (resonators) on the same device. To isolate the sensors from each other, a gap of 1 mm was left between the etch pits (1mm) of our resonators.

The energy trapping in such inverted MESA structures can be explained by the total internal reflection of vibrations from the edge of the electrodes. If the electrode diameter to the crystal thickness ratio of the resonator is large, there is more energy trapping and it results in a higher Q-factor. However, if this ratio is small, there is a large leakage of the acoustic energy through the wafer volume. If this ratio is small, poor Quality factors are observed in resonators. Hence to maximize the quality factor, it is necessary that we increase the electrode diameter.

However for the suppression of the spurious modes the rule of thumb expression relating the quartz thickness and the radius of electrodes is given by [4]

$$\Delta f_{pb} < f_o \cdot \frac{2.337}{N^2}\left(\frac{d}{r}\right) \qquad \textbf{2.1}$$

Where, f_o is the resonance frequency of the quartz resonator after the mass loading due to the electrodes, f_{pb} is the plate back frequency i.e., the frequency difference between the resonance frequency of the bare crystal and after the deposition of top and bottom electrodes. ‘d’ is the thickness of the resonator and ‘r’ is the radius of the electrode deposited. We can see from the above equation that as the thickness of the resonator decreases it is necessary for us to reduce the radius of the electrodes in order to suppress the spurious modes. These opposing constraints require a design compromise.

In order to find the best electrode diameter to the thickness ratio of our resonators, we designed a mask with different electrode sizes (Figure **2-1**) to test the best ratio for the suppression of the spurious modes. In our tests, it was found that an 800 μm top electrode with a 500 mm diameter bottom electrode gave us the best results for the 18.5 μm thick resonator and resulted in the least number of spurious modes, while giving the highest quality factor.

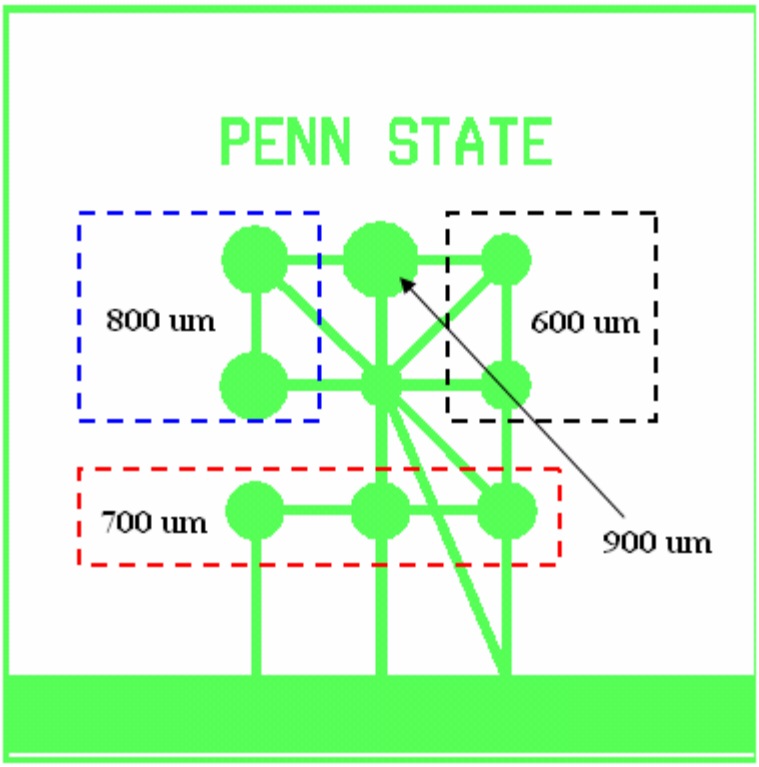

Figure 2-1:Mask with Variable Electrodes

In addition to the etching of the pixel, we also etched a path for the signal conduction. Gold lines carry the electrical signal to the bonding pads. The bonding pad is partially etched so the unetched (robust) part of the pad can be used to wire bond the device to the package. However due to the geometry of the etched pattern, the etch side lithography has got some defects. This is seen due to the diffraction of the light from the edges of the etch pattern. This results in spots of gold that remain protected by the photoresist during the gold-etch. In order to reduce the contribution of this gold along the signal conduction lines to the spurious modes, we burnt off the excess gold along these lines and in the

pixel by using a laser gun. This caused sharper peaks and reduction of the spurious modes while improving the quality factor as shown in Figure 2-2

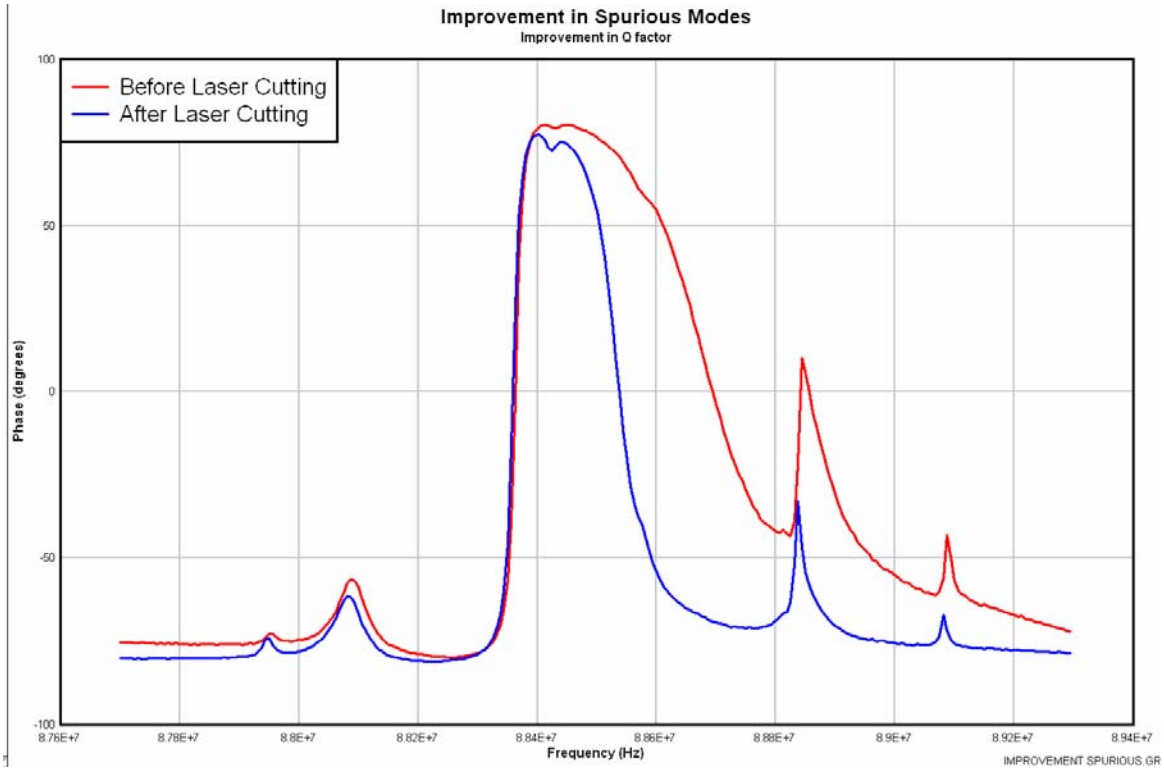

Figure 2-2: Spurious Mode separation and Improvement of the Q factor due to Laser cutting

2.2: Fabrication of the Quartz Resonator Array

We obtained one inch diameter Y-cut quartz wafers with double-sided polish from Boston Piezo-Optics. To ensure ease of handling and increasing yield, we fabricated 4

square dies (9mm) on each quartz wafer. Each die had 8 resonators of 1mm diameter. Thus each die has 8 resonators and can thus be used for parallel measurement.

The Steps in the fabrication of the devices are as outlined below.

2.2.1: Cleaning and First Lithography

The Quartz wafers obtained from Boston Piezo-Optics were cleaned using Acetone (10 mins) and Iso-Propyl Alcohol (IPA – 10 mins) followed by a De-Ionized (DI) water rinse. They were then immersed in Pirhana (H_2SO_4:H_2O_2:: 1:1) for 60 mins to ensure that the wafers were thoroughly cleaned.

The wafer was then mounted using Shipley® Photoresist 1805 on a perforated glass wafers and then baked at 110^o C for 5 minutes. We use perforated glass wafers to ease the demounting of the quartz wafers. If the quartz wafers were mounted on plain glass wafers it took 3 days for the demounting.

Shipley® Photoresist 1827 was then patterned on the quartz wafers using mask 1 as shown in **Figure 2-3** which defines the quartz etch pattern.

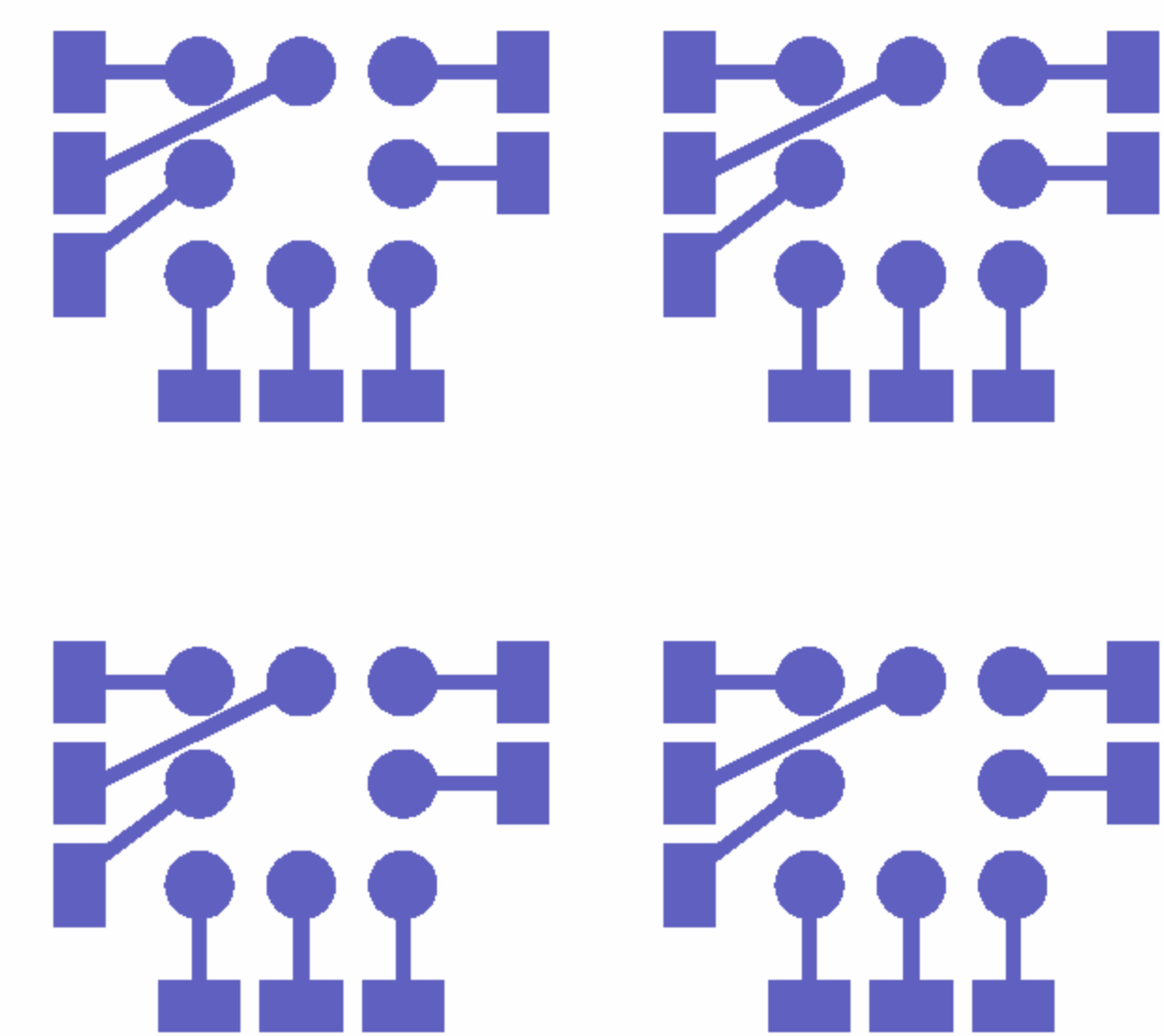

Figure 2-3: Mask 1: Quartz Etching Pattern

Gold was then evaporated using Chrome as an adhesion layer to form the seed layer for Electroplating. The Gold was patterned on the wafer using the Lift-Off process.

One die of the wafer at this stage can be shown as in Figure 2-4

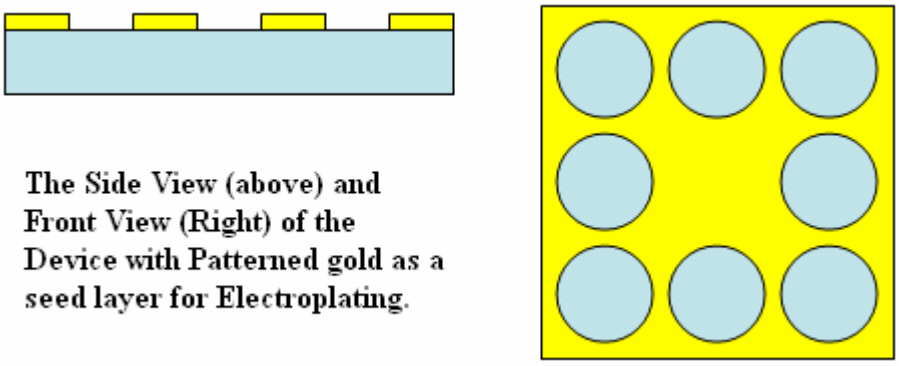

The Side View (above) and Front View (Right) of the Device with Patterned gold as a seed layer for Electroplating.

Figure 2-4: Patterned Gold as a seed layer for Nickel Electroplating

The wafers were then demounted and mounted with the patterned layer down. A blank Gold evaporation was then done with Chrome as an adhesion layer. This was to aid the mounting of the wafer with Indium for etching as described below. The wafers were then demounted and then remounted with the patterned side up on a glass slide with gold on one side.

The wafers were electroplated with nickel as shown in Figure 2-5 which acted as a hard mask during to the etch process.

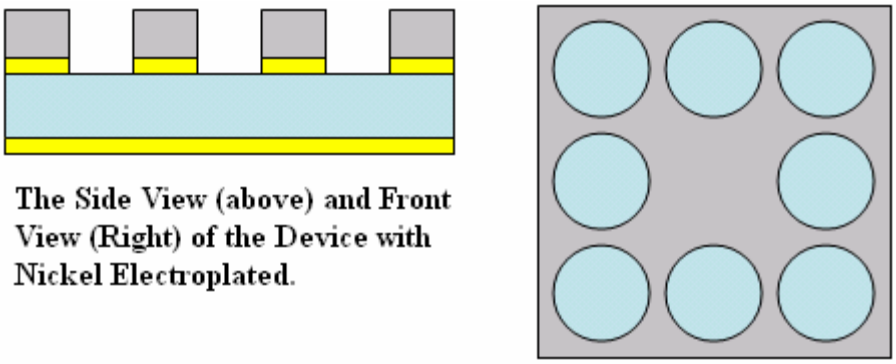

The Side View (above) and Front View (Right) of the Device with Nickel Electroplated.

Figure 2-5:Wafer with Nickel Electroplating

The nickel was electroplated for 45 minutes at a current of 35 mA to give a thickness of about 12 um using a pulsed power supply with a frequency of 10 Hz and a duty cycle of 80%. The Ni-electroplating solution obtained from Alfa Aeser™ Ltd was constantly stirred using a magnetic stirrer. In order to ensure a fine grain size, a dummy electroplating run was always preformed under the same conditions for 35 minutes. This ensured that the deposited metal had a fine grain size.

2.2.2: Etching

In order to etch the electroplated wafers, they were mounted on 4-inch Silicon wafers using an Indium-Tin solder alloy. Using this alloy caused a cushion between the thermal expansion of silicon and quartz and any other mounting medium as photo resist. This

alloy absorbed all thermal stresses and the wafers survived long etch times. Other mounting mediums caused the wafers to crack within two hours of etching.

The wafers were etched using an inductively coupled plasma (ICP) at RF power 2000W, Substrate power 400W with an Ar flow rate of 50 sccm and an SF_6 flow rate of 5 sccm [2][3]for about 4-5 hours. The etched wafers were then demounted from the mounting silicon wafers by placing them on a hot plate at 150^{o}C and melting the indium-tin solder and sliding off the wafers carefully using a very small tangential force. The quartz wafers were then cleaned using aqua regia (HCl: HNO_3:: 3:1) to stip off the gold, nickel and any remaining residues of the indium –tin alloy. The device at this stage looked as shown in Figure **2-6**

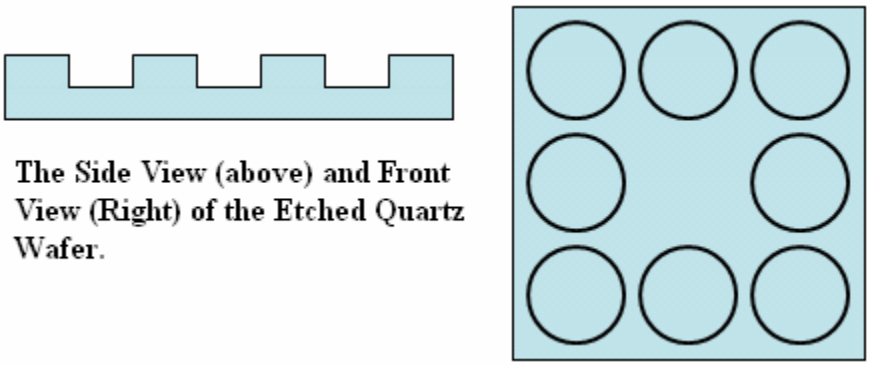

The Side View (above) and Front View (Right) of the Etched Quartz Wafer.

Figure **2-6**: Etched Quartz

2.2.3 Dicing

The Etched wafers were too fragile to survive the next lithography steps and are hence diced into 4 individual dies (devices). During dicing, to protect the wafers from the mechanical shearing force of the blade cutting the wafer and of the cooling water jet, the quartz wafers were each mounted on a perforated glass wafer using Micro Chem Photoresist SU-50. Shipley® Photoresist 1827 was spun on the wafers to trap the particles generated during the dicing process.

The diced wafers were then cleaned and demounted in acetone, giving 4 individual 9mm square dies.

2.2.4: Second Lithography: Definition of the Etch Side Electrodes

The cleaned wafers were mounted on a perforated Glass wafer using Shipley® Photoresist 1805. Gold (1000 A) was then evaporated on the wafers using an adhesion layer of Chrome (100 A). This gold acted as the etch side electrode also referred to as the back-side of the device.

Mask 2 (Figure 2-7) was then used to pattern the gold (etching) using Shipley® Photoresist 1827 on Aligner EV601.

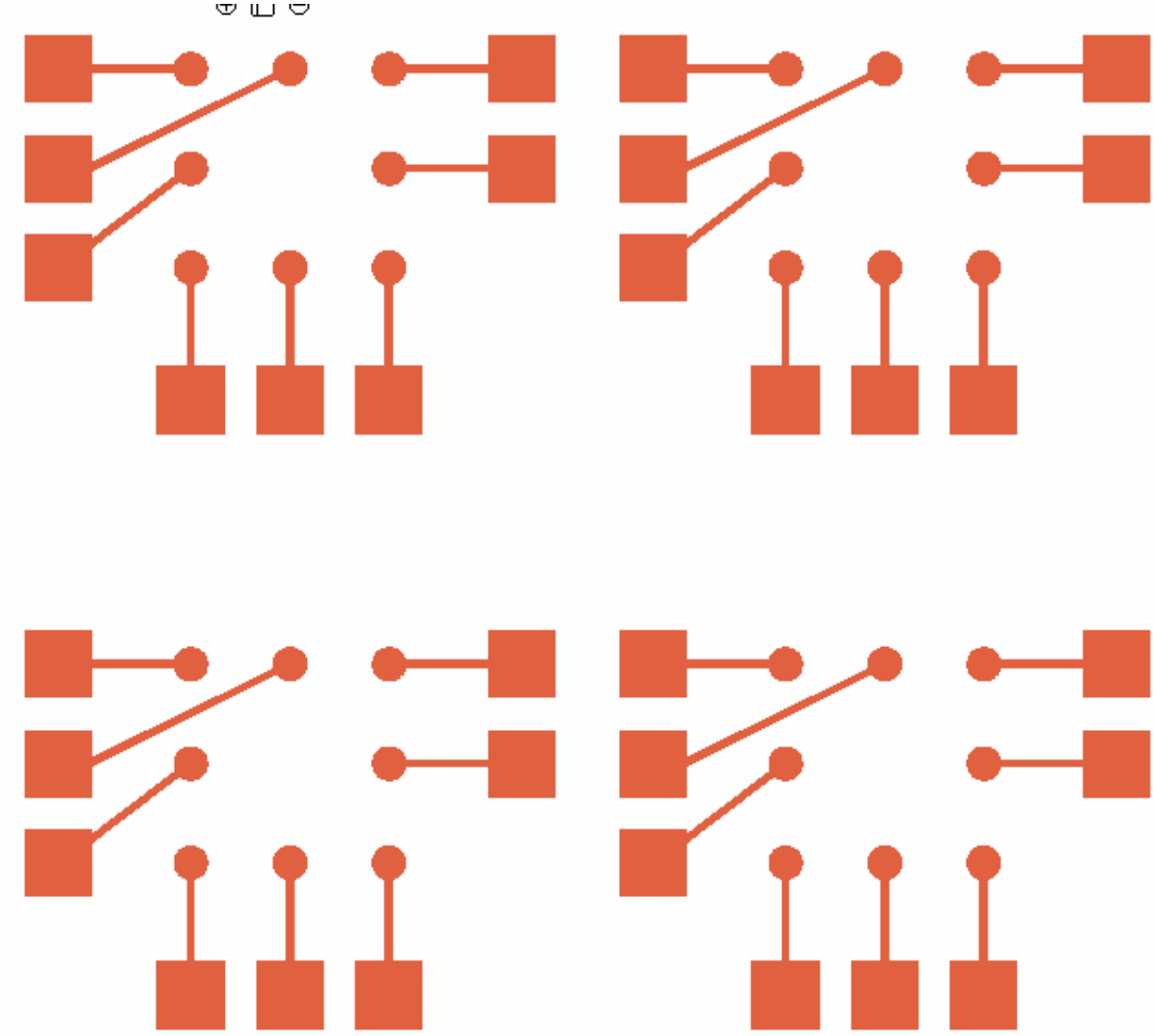

Figure 2-7: Mask 2: Etch Side Electrode Definition

The device now looked as shown in Figure 2-8 . However it is important to note that the schematic of the device concentrates on the resonator pixel and does not include the signal conduction lines as shown in the mask.

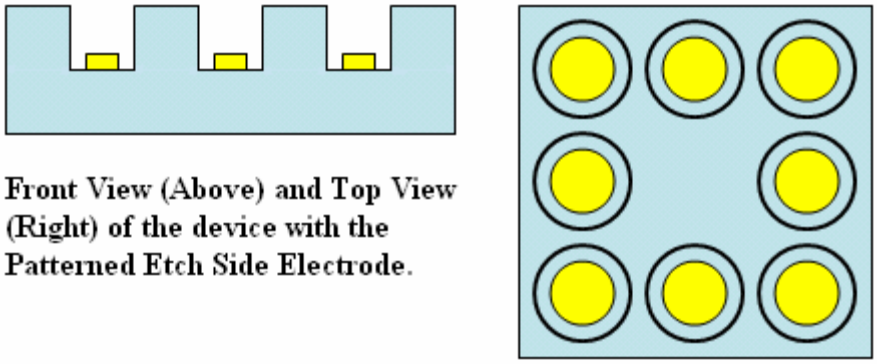

Front View (Above) and Top View (Right) of the device with the Patterned Etch Side Electrode.

Figure 2-8: Device with Patterned Etch Side Electrode

2.2.5 Third Lithography: Definition of the Front Side Electrodes:

The wafers were demounted using acetone and remounted on glass slides using Shipley photoresist 1805 with the etch side down. Mask 3 (Figure 2-9) was used to pattern the front side electrodes by using a bilayer lift-off process using Micro Chem resists LOR 5A and SPR 3012.

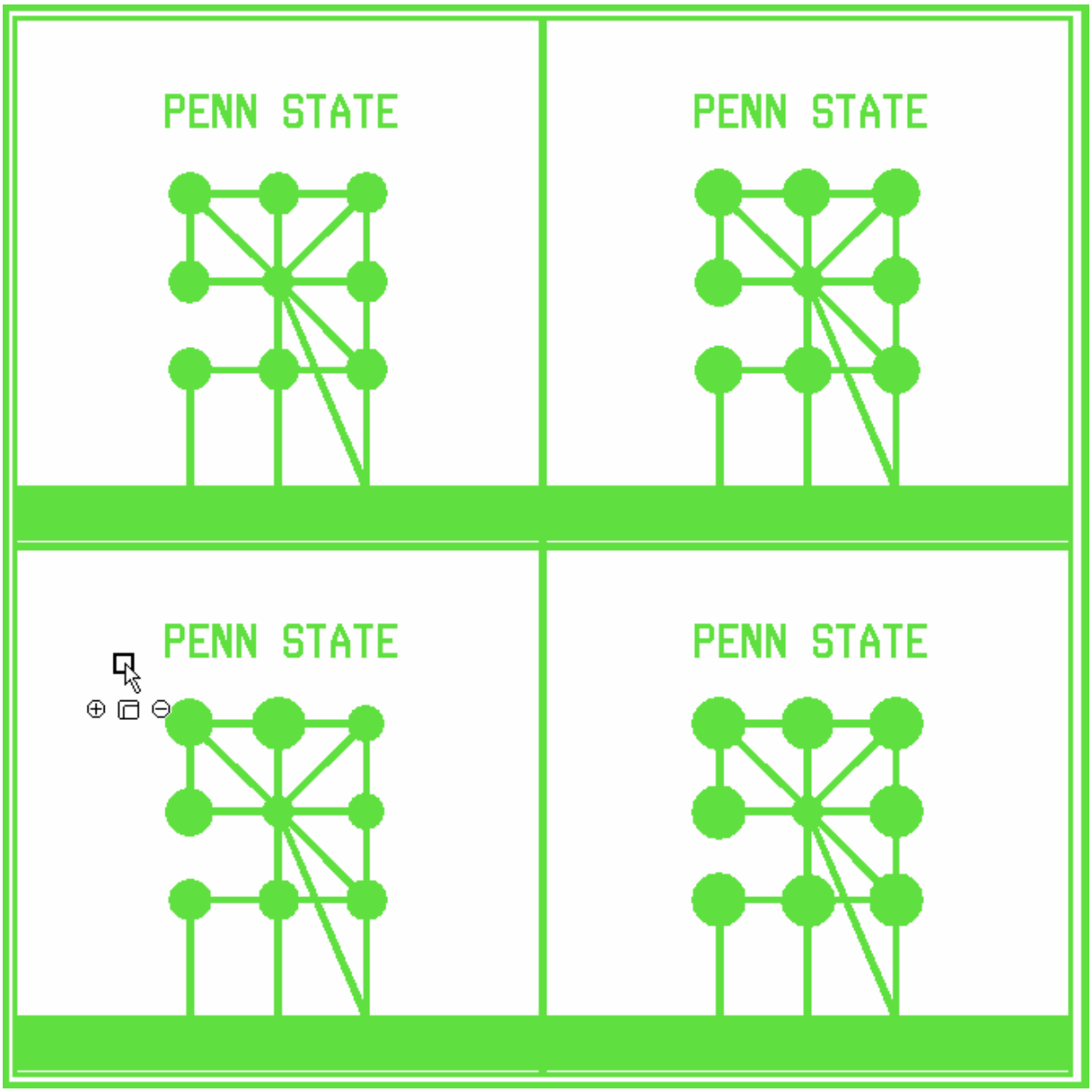

Figure 2-9: Mask 3: Definition of the Front Side Electrode

This was the final step in the fabrication of the device. The fabricated device can be shown as Figure 2-10

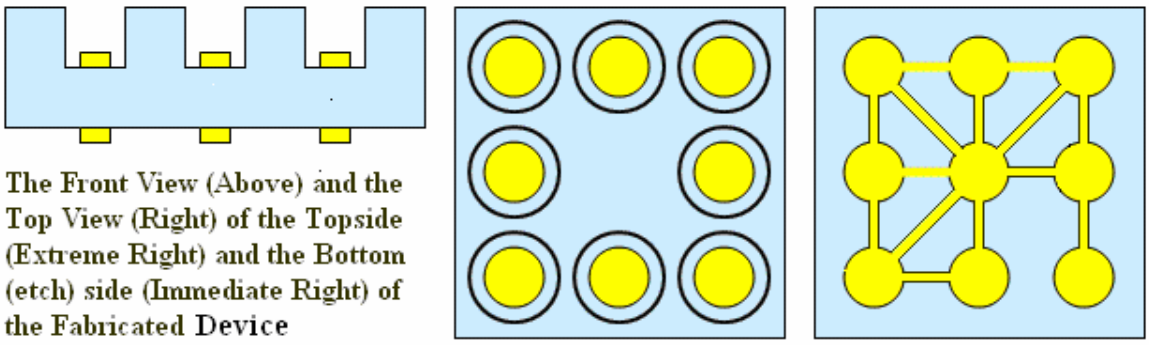

The Front View (Above) and the Top View (Right) of the Topside (Extreme Right) and the Bottom (etch) side (Immediate Right) of the Fabricated Device

Figure 2-10: The Fabricated Device

The optical photograph of the fabricated device can be shown as Figure 2-11

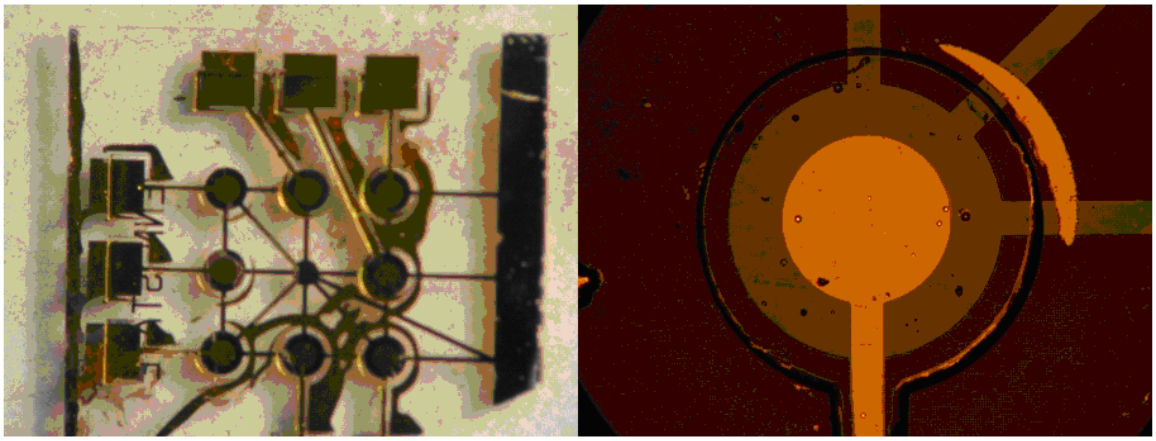

Figure 2-11: Optical photograph of the fabricated device and the close up of one pixel

2.2.6: Packaging of the Device

The fabricated device was packaged in a 24 PIN DIP ceramic package obtained from Spectrum Semiconductors Ltd. A 5mm square hole was drilled in the centre of this package by water jet machining. We then packaged the fabricated resonator array by placing its flat side down on the hole and using a ring of silicone glue around the drilled hole as an adhesive. The glue was allowed to cure for about 24 hours. The electrical connections to the etched side of the QCM were then made using a wire-bonder. The common electrode was connected to the gold on the package by using a silver paste. The packaged device is as shown below in Figure **2-12**

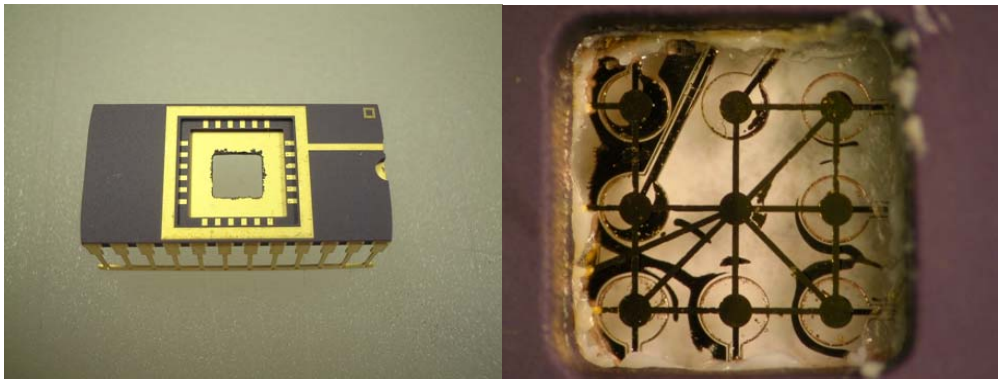

Figure **2-12**: Package and Packaged device

The device is now ready to be calibrated and tested as a thermal sensor.

1. *Morio Onoe 'Effect of Energy Trapping on Performance of QCM' 0-7803-9052-0/05/ © 2005 IEEE*

2. *Abhijat Goyal 'Ultrasensitive Quartz Crystal Microbalance Integrated With Carbon Nanotubes'* Penn State University August 2006

3. *Ping Kao 'Fabrication And Analysis Of Raman Active Micro QCM Sensor Arrays* Penn State University Dec 2006

4. Lucklum, R.; Eichelbaum,F. Interface circuits for QCM sensors. In *Piezoelectric Sensors*; Steinem, C., Janshoff, A., Eds.; Springer Verlag: NewYork, 2007; pp 3-47

Chapter 3

Characterization of Micromachined Y-Cut Resonators

In this Chapter the resonance parameters measured from the fabricated Y-cut resonators are compared to the theory discussed in Chapter1. Calibration data for the temperature-sensitivity of the micromachined resonators will be presented next. Finally, the application of the micromachined Y-cut quartz resonators for infrared radiation sensing is presented as an example of thermal sensors.

3.1 Measurement of the Resonance Characteristics of the Fabricated Resonator

An Agilent impedance analyzer (4294A) was used to measure the impedance as a function of frequency of the micromachined quartz resonator. Prior to the measurement, open, short, and 100Ω load based compensation was used to minimize all extraneous contribution to the impedance arising from the test set-up. Frequency sweep spanning an appropriate range suitable for the specific resonance characteristic was determined and all measurements were made to measure the impedance and the phase (theta). The efficacy of the compensation was determined by comparing the experimentally observed impedance just off the resonance peak and comparing it with the impedance calculated using a parallel plate based capacitor model approximation for the device.

The parallel plate capacitor (C_0) off the resonance peak can be calculated as Eq. **3.1**

$$C_o = \frac{\varepsilon_o \varepsilon_r A}{d} = 441\, fF \qquad \textbf{3.1}$$

where, $\varepsilon_o = 8.854 \times 10^{-12}$ is the permittivity of free space, $\varepsilon_r = 4.7$ is the relative permittivity of quartz as given by Boston Piezo-Optics Inc, A is the area of the pixel and d is the thickness of the quartz resonator. The calculated capacitance at resonance results in impedance (Z) as given by Eq. **3.2**

$$Z = \frac{1}{j\omega C_o} = 4049.78\Omega \qquad \textbf{3.2}$$

The impedance variation of the device with frequency can be plotted as Figure **3-1** . We can see that the impedance seen on the device is much lesser (956.199Ω). Using this value to calculate Co, we get

$$C_o = \frac{1}{j\omega Z} = 1.87\, pF \qquad \textbf{3.3}$$

This can be explained due to the stray parasitic capacitances present in the packaging.

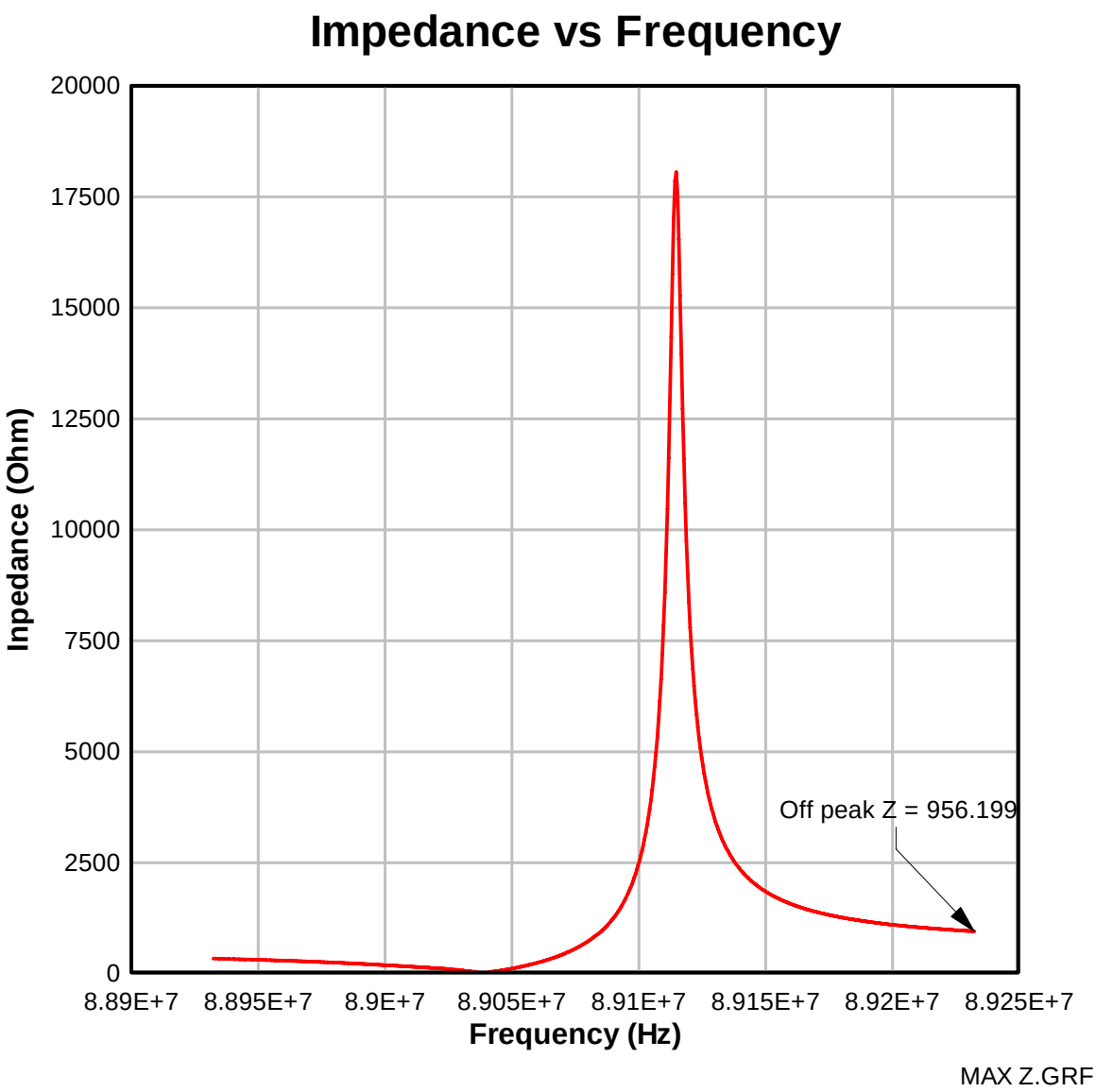

Figure **3-1**: Impedance vs. frequency curve for the quartz resonator.

To ensure that the compensation of the impedance analyzer was sufficiently accurate, a resistor was measured in the desired frequency range and the measurement error was 4.78×10^{-5} % . We know that we have etched down to about 18 μm (d) during the etch process mentioned in Chapter 2. This should give us a resonant frequency (f_o) of about 90.2 MHz as explained by Eq. **3.4**

$$f_o = \sqrt{\frac{\mu_q}{\rho_q}} \times \frac{1}{2d} = 90.2\ MHz \qquad \textbf{3.4}$$

Where, ρ_q is the density of quartz = 2.768 g/cm ^{3} and μ_q is the shear modulus of quartz = $2.9478*10^{11}$g/cm^2.

A typical phase spectrum around resonance is shown in Figure **3-2** . We can see that the resonance frequency is about 89 MHz as estimated. The phase change from between -90 degrees and +90 degrees agrees well as the phase change between the series and parallel resonance.

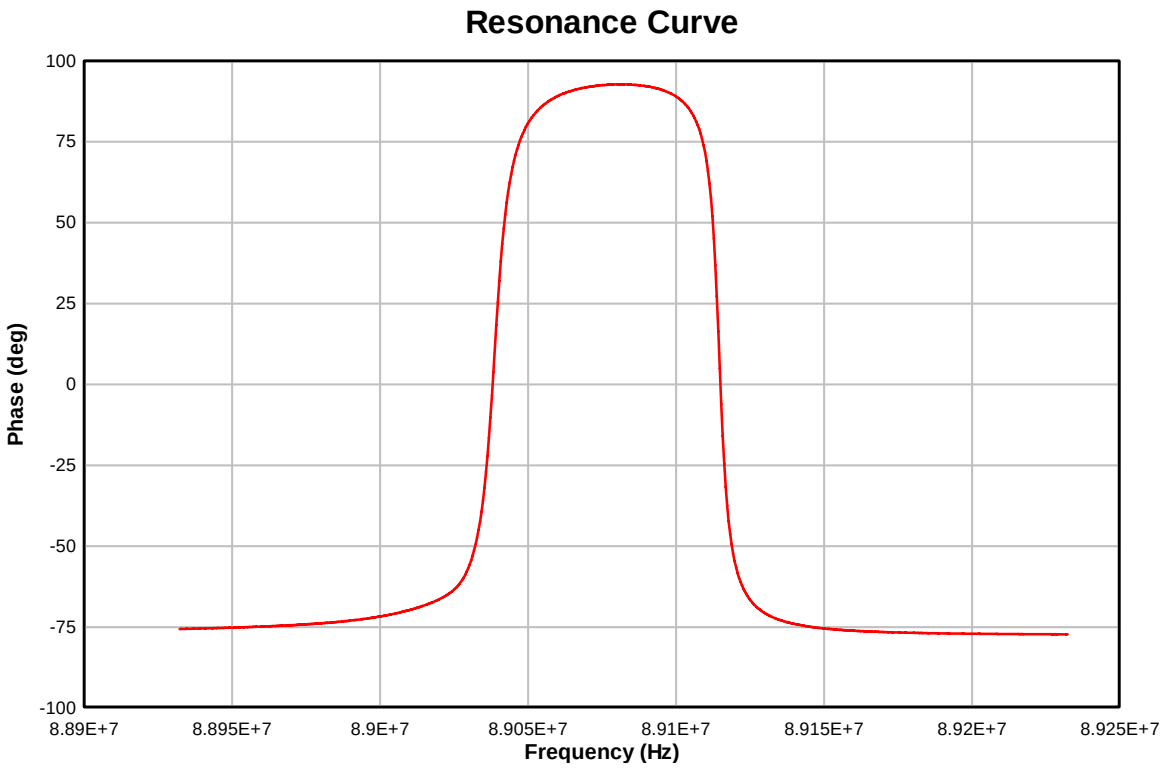

Figure **3-2**: Resonance Curve for Device A

The impedance analyzer was set-up to the BVD equivalent circuit representation for the quartz resonator and the equivalent circuit parameters were calculated using the

Agilent impedance analyzer algorithms. The parameters from the impedance Analyzer are recorded as:

Table 3-1: Resonance Parameters of the device

Parameter	Value
R_m	33.9367 ohm
L_m	0.691mH
C_m	4.63fF
C_o	2.67pF

We shall compare the resonance parameters of this curve with the equations derived in Chapter1. In order to plot the various frequencies, we plot the Admittance circle (Figure 3-3) of this resonance curve and compare the value to the obtained motional resistance.

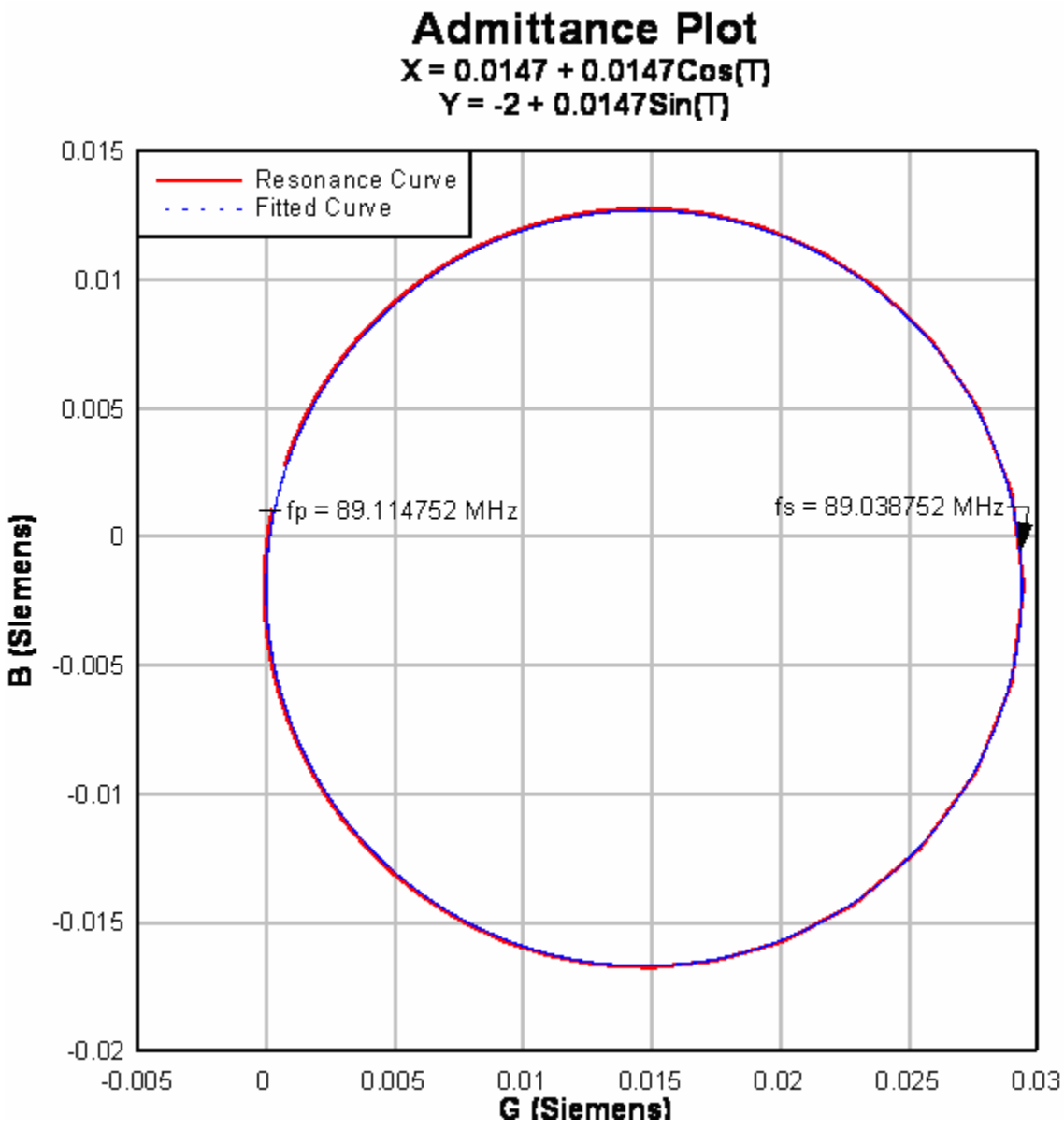

Figure **3-3**: Admittance (Y= G + jB) plot of the resonance curve.

Comparing the plotted equation of the circle with the equation of the circle with Chapter 1, The radius of the circle is $\frac{1}{2R_m} = \frac{1}{2 \times 33.9367} = 0.0147$ Siemens which is an exact match and the centre is at $\left[\frac{1}{2R_m}, \overline{B_o}\right] = \left[0.0147, 1.49 \times 10^{-3}\right]$, However that of the

Plotted Circle is at $\left[0.0147,\ 2\times10^{-3}\right]$. This difference is due to a mismatch between the calculated capacitance (C_o) and the recorded value of C_o by the Impedance Analyzer ($\overline{B_o}=\omega_s\times C_o$). We can compare the other parameters observed and calculated as shown in Table **3-2** .We can see that the observed and calculated parameters are in excellent agreement with theory. The only large error is in the k^2 value which can also be explained by the large difference in C_0 due to the presence of parasitic capacitances.

Table 3-2: Comparison of the resonance parameters for the device

Parameter	Observed	Calculated/ Theory	Error
f_s	89.038752MHz	$\frac{1}{2\pi}\sqrt{\frac{1}{L_m C_m}}\left(1+\frac{C_o R_m^2}{2L_m}\right)$ $= 88.979831\ MHz$	- 0.066%
f_p	89.114752 MHz	$\frac{1}{2\pi}\sqrt{\frac{1}{L_m C_m}}\left(1+\frac{C_m}{2C_o}-\frac{C_o R_m^2}{2L_m}\right)$ $= 89.056854\ MHz$	- 0.065%
f_{Zmin}	89.037996 MHz	$\frac{1}{2\pi}\sqrt{\frac{1}{L_m C_m}}\left(1-\frac{C_o R_m^2}{2L_m}\right)$ $= 88.979435\ MHz$	- 0.065%
f_{Zmax}	89.115248 MHz	$\frac{1}{2\pi}\sqrt{\frac{1}{L_m C_m}}\left(1+\frac{C_m}{2C_o}+\frac{C_o R_m^2}{2L_m}\right)$ $= 89.056190\ MHz$	- 0.066%
$f_s - f_{Zmin}$	756 Hz	396 Hz	360 Hz
$f_{Zmax} - f_p$	496 Hz	394 Hz	102 Hz
ω_s	559.4469 MHz	559.0767 MHz	- 0.066%
ω_p	559.9245 MHz	559.5607 MHz	- 0.065%
Q -Factor		$Q = \frac{\omega_s L_m}{R_m} = 11416.5$	
Velocity(v_a)	$v_a = \frac{d \times \omega_p}{\pi} = 3297.26\ \frac{m}{s}$	3334m/s	1.01%
k^2	$\frac{\omega_p - \omega_s}{\omega_p} = 4\ \frac{k_T^2}{\pi^2}$ $k_T^2 = \frac{k^2}{k^2+1} = 2.1387 \times 10^{-3}$	8.5×10^{-3}	74.85%

Initially we tried to functionalize the resonator surface to try preliminary calorimetric sensing of biochemical reactions. The addition of various chemicals and enzymes on the surface of the device left a residue and could not be completely cleaned. This caused an increase in the motional resistance (R_m) and a reduction in the Q-factor of the device. The characteristics of this device were now measured and can be shown as Figure **3-4**

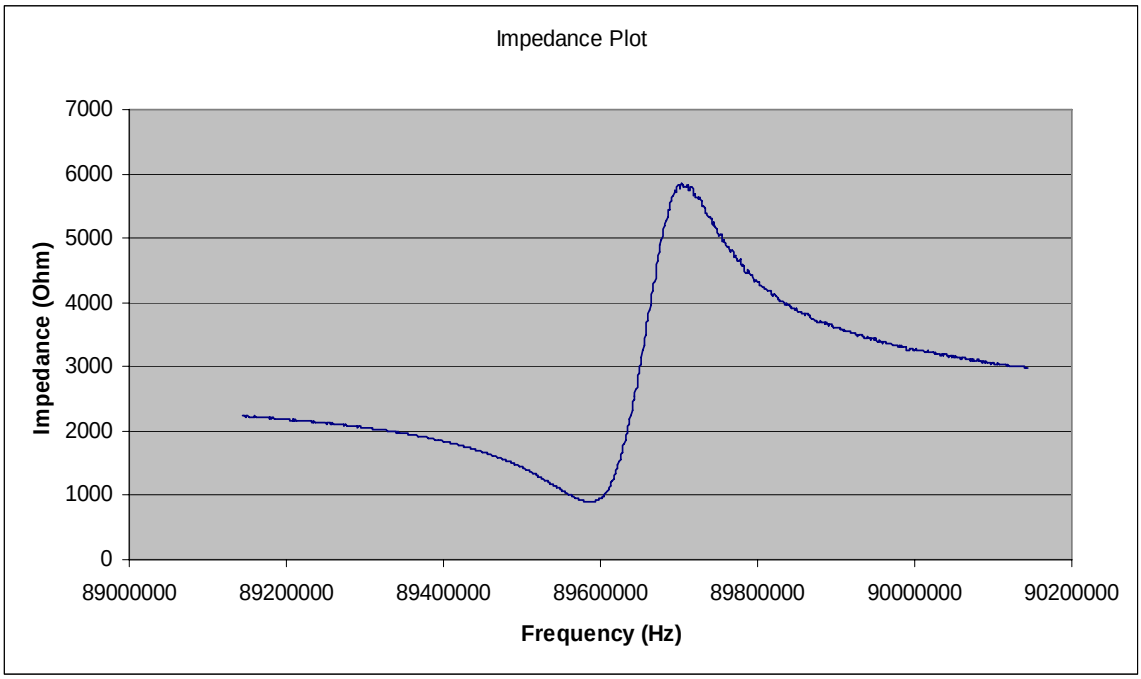

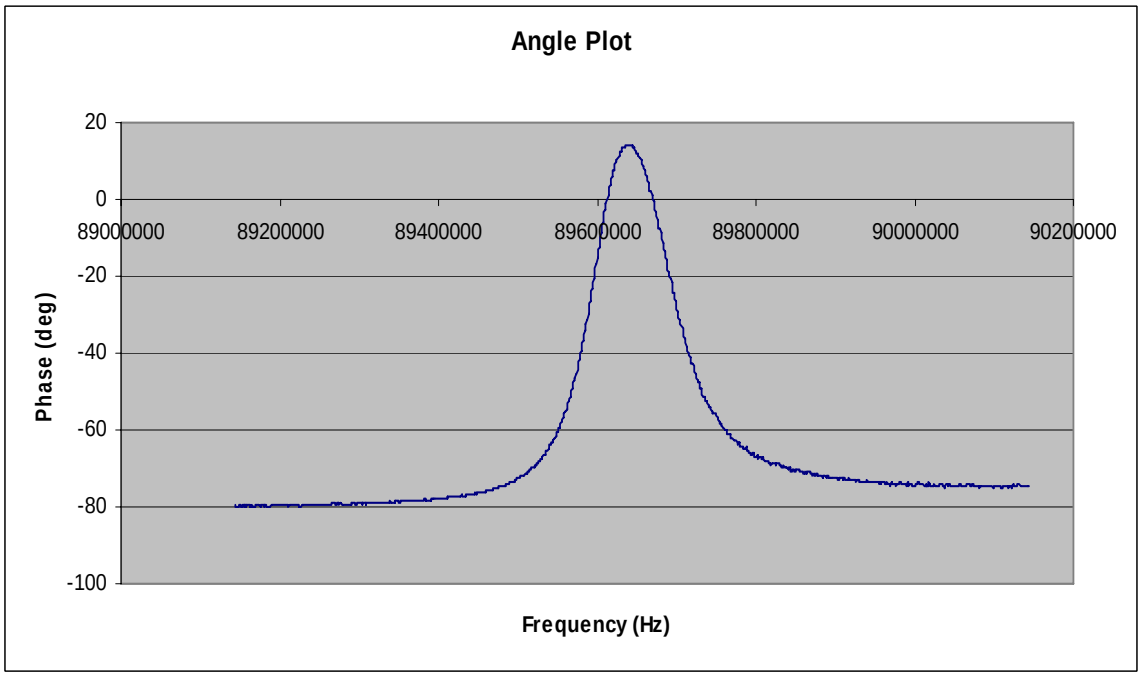

Figure 3-4: Measured Impedance and Angle spectra for the Fabricated Device.

The curve shown in Figure 3-4 was fit to a standard Lorentzian function, (Figure 3-6) which represents the solution to the differential equation of a forced

resonance to calculate the Quality factor of the QCM. A Mathematica® program was written to do this fitting. This program is attached in Appendix B

The Lorentzian function can be written as: Eq. **3.5**

$$a0 + \frac{A\left(\frac{f\,\mathrm{Cos}[\mathrm{phi}]}{fo} + \left(1 - \frac{f^2}{fo^2}\right) Q\,\mathrm{Sin}[\mathrm{phi}]\right)}{\frac{f^2}{fo^2} + \left(1 - \frac{f^2}{fo^2}\right)^2 Q^2} \qquad \textbf{3.5}$$

where, f is the frequency of the point, f_o is the estimated resonance frequency, Q is the estimated quality factor and phi represents the phase of the point to be fitted. The fitted curve for the fabricated device is as shown in Figure **3.6**. The Q factor obtained from the fit was 813.711. This shows a very high reduction in the Quality factor of the resonator. The ANOVA table for the generated fit is as shown in Figure **3-5**.As can be seen from the Mean squared error (2.00371), a good fit of the resonance curve is obtained.

		DF	SumOfSq	MeanSq
	Model	5	3.72456×10^6	744 911.
$Q \to -813.711, A \to 98.1028\}$,	Error	795	1592.95	2.00371 $\}\}$[[1, 1]]
	Uncorrected Total	800	3.72615×10^6	
	Corrected Total	799	470 246.	

Figure **3-5**: ANOVA table for the lorentzian fit

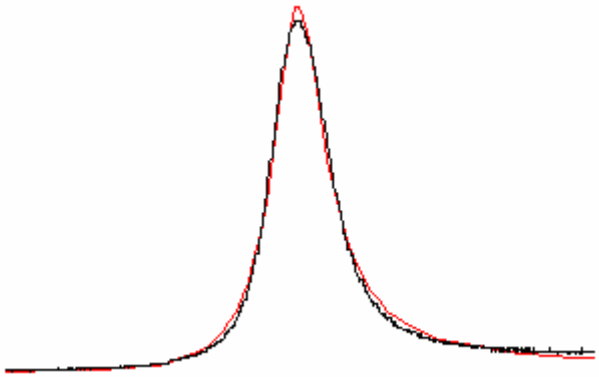

Figure 3-6: Resonance curve (black) fitted with the lorentzian curve (red)

The parameters from the impedance Analyzer for the BVD Equivalent circuit were as shown in Table 3-3

Table 3-3: Resonance parameters recorded from the Impedance Analyzer

Parameter	Value
R_m	1.0599k
L_m	1.8mH
C_m	1.75231fF
C_o	734.432fF

The admittance plot for the resonance curve is plotted as shown in Figure 3-7 (red). The respective curves are fitted with the equation for the circle as discussed earlier. We can show that the plotted curve has a slightly different equation from the expected theoretical equation.

Table 3-4

Table 3-4: Expected and Fitted Admittance Circle Parameters

Theoretical	Fitted	Error
Radius = $\frac{1}{2R_m} = 4.717 \times 10^{-4}$	4.717×10^{-4}	0%
$\overline{B_o} = 4.135 \times 10^{-4}$	3.4135×10^{-4}	17.44%

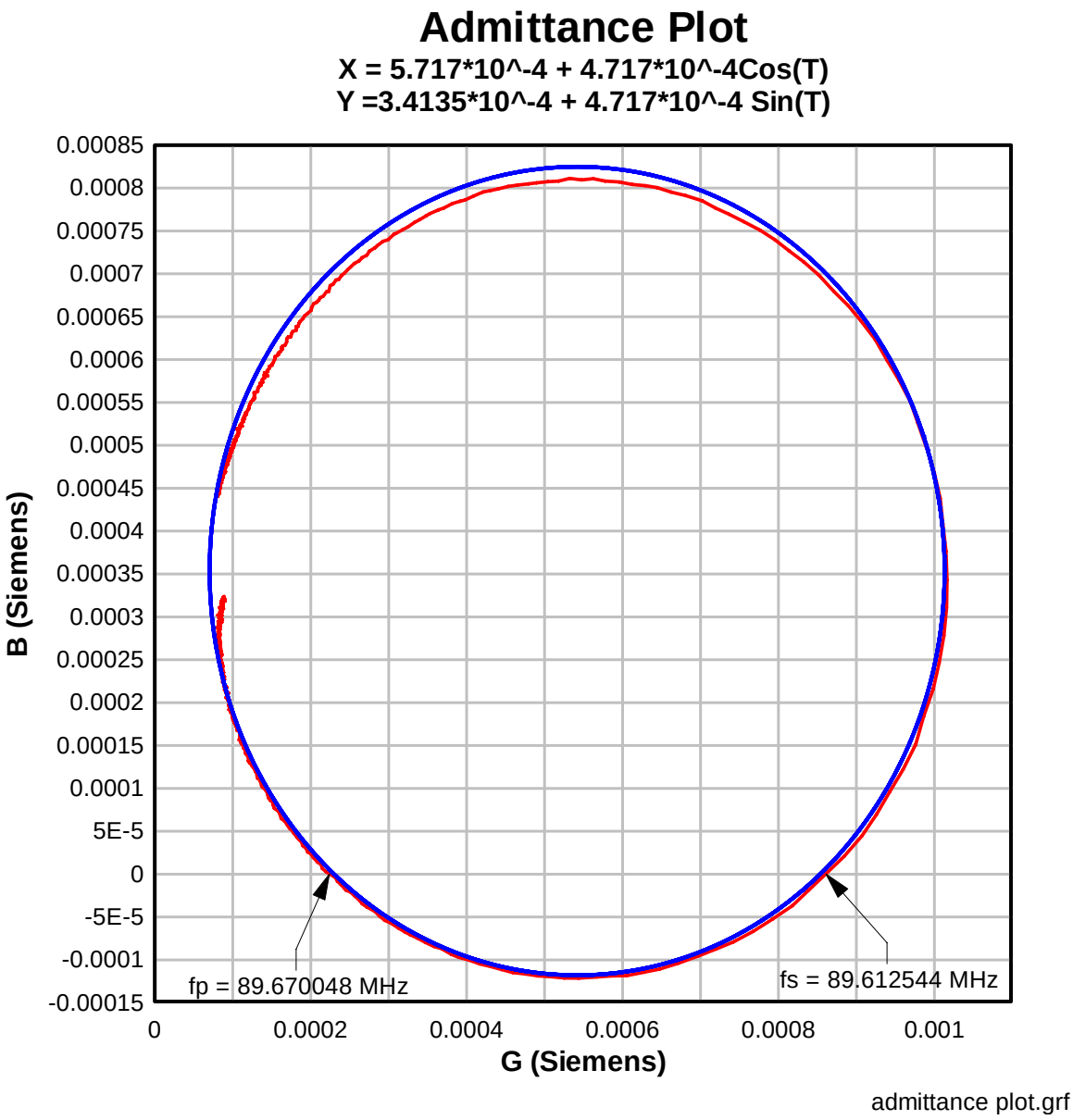

Figure 3-7:Impedance and Admittance Plot of the resonance curve

We can compare the parameters observed and calculated as shown in Table 3-5 .We can say that the errors in this scenario are larger. This is due to an increase in the motional resistance (R_m- which affects the Q factor) and a mismatch in the value of the plate capacitance (C_o).

Table 3-5: Comparison of the resonance parameters

Parameter	Observed	Calculated/ Theory	% Error
f_s	89.612544 MHz	$\frac{1}{2\pi}\sqrt{\frac{1}{L_m C_m}}\left(1+\frac{C_o R_m^2}{2L_m}\right)$ $= 89.694182\ MHz$	0.09%
f_p	89.670048 MHz	$\frac{1}{2\pi}\sqrt{\frac{1}{L_m C_m}}\left(1+\frac{C_m}{2C_o}-\frac{C_o R_m^2}{2L_m}\right)$ $= 89.700833\ MHz$	0.034%
f_{Zmin}	89.587552 MHz	$\frac{1}{2\pi}\sqrt{\frac{1}{L_m C_m}}\left(1-\frac{C_o R_m^2}{2L_m}\right)$ $= 89.593997\ MHz$	0.0071%
f_{Zmax}	89.703848 MHz	$\frac{1}{2\pi}\sqrt{\frac{1}{L_m C_m}}\left(1+\frac{C_m}{2C_o}+\frac{C_o R_m^2}{2L_m}\right)$ $= 89.848846\ MHz$	0.16%
$f_s - f_{Zmin}$	24992 Hz	100785	75.2%
$f_{Zmax} - f_p$	33800 Hz	148013	77.16%
ω_s	563.052 MHz	563.565 MHz	0.091%
ω_p	563.4135 MHz	563.606 MHz	0.034%
Q -Factor	813.711	$Q = \frac{\omega_s L_m}{R_m} = 956.7$	14.94%
Velocity(v_a)	$v_a = \frac{d \times \omega_p}{\pi} = 3322.89\ \frac{m}{s}$	3334m/s	0.33%
k^2	$\frac{\omega_p - \omega_s}{\omega_p} = 4\frac{k_T^2}{\pi^2}$ $k_T^2 = \frac{k^2}{k^2+1} = 5.89 \times 10^{-3}$	8.5×10^{-3}	30.7%

We can see from Table **3-5**, that the highest error is in the frequency shift of the various resonance frequencies. This is because these frequencies depend on the parallel plate Capacitance. The dependence of the resonance characteristics on the motional resistance and the capacitance is as shown in Figure **3-8** . An increase in the damping (motional resistance R_m) causes a shift in the resonance curve. This resistance represents the losses in the crystal due to ohmic and acoustic losses in the quartz and the metallic layers. We can see from Table **3-3** that the value of motional resistance is too high (~1k) in this particular resonance. This causes a reduction in the qualify factor of the resonator. For optimal operation, as seen in the earlier resonance curve the value of the motional resistance should be below 50Ω [**5**].A mismatch in the parallel plate capacitance has an influence in the maximum off peak resonance of the quartz resonator and changes the parallel resonance frequency. Hence, in this case, an exact fit is not achieved for the admittance circle as predicted by theory.

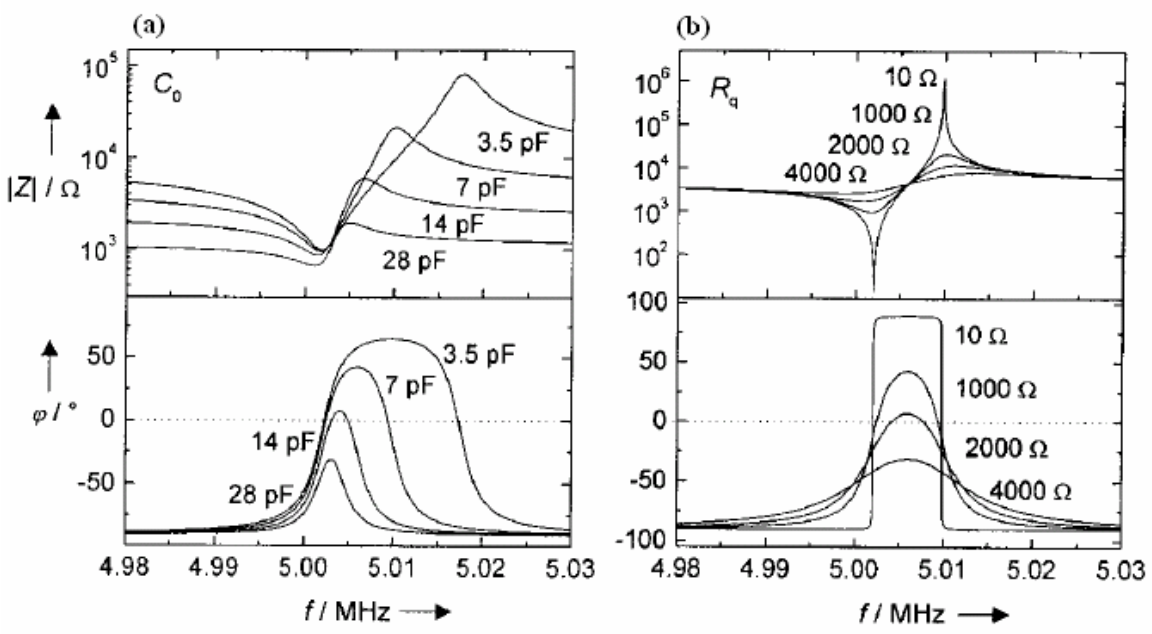

Figure **3-8**:Simulated Spectra from the Butterworth-van Dyke model with discrete variation of C_o (a) and R_m (b) [**6**]

3.2 Temperature Calibration of the Fabricated Devices:

The fabricated devices were then calibrated for sensitivity to temperature from room temperature to about 60°C. Typically the operating temperature range of thermal sensors does not exceed this temperature range and was therefore considered to be adequate. The packaged device was placed in an oven and temperature was allowed to stabilize. The frequency readings were taken at periodic intervals, at stabilized temperatures using an Agilent impedance analyzer 4295A. The frequency drift with temperature was measured and plotted for 4 different devices. This is shown below in Figure **3-9** .

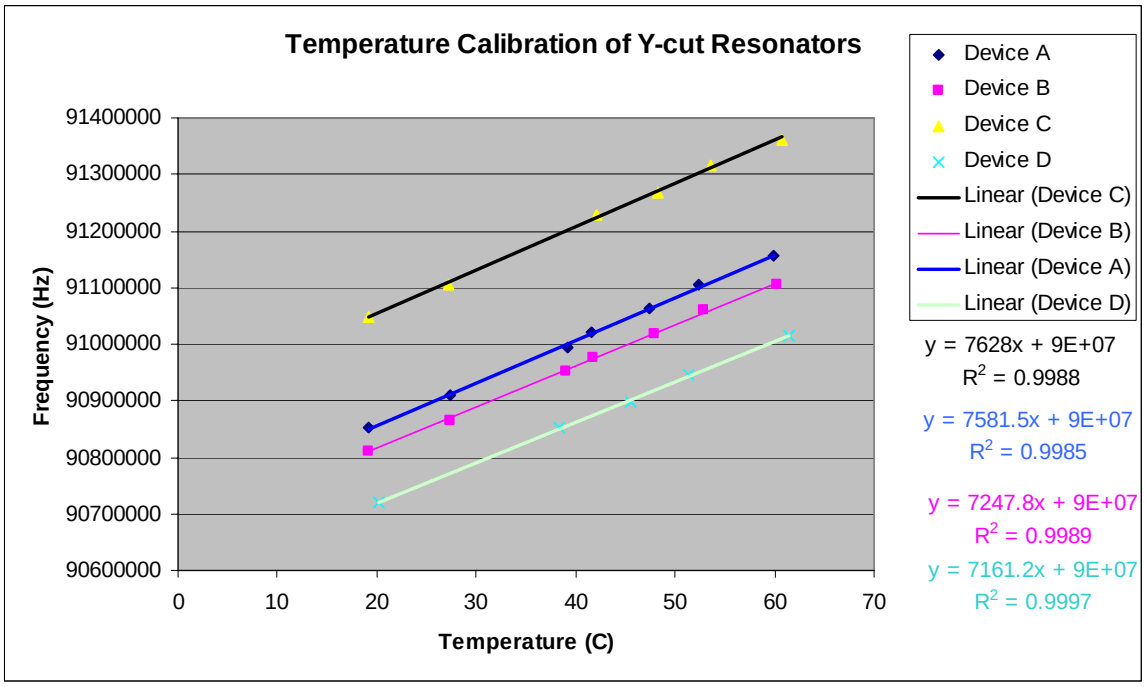

Figure 3-9: Device A Calibration Chart

As we can see from the above figure, we can see a linear rise in frequency with increase in temperature in all the resonators with a very similar slope. We get a shift of 7.1 to 7.6 kHz/^{o}C (80 – 85ppm/^{o}C) for the resonators. Thus, the sensitivity of the devices to change in temperature is calibrated. The closeness of the slopes in the above graph is a measure of the accuracy of the calibration.

From the choice of the Y-cut of quartz we know that it has a sensitivity of ~90ppm/^{o}C [1]. For a 90 MHz resonator, we should have about 8100Hz/^{o}C. Our devices have a good match with this number and the deviation can be attributed to manufacturing method and packaging of the devices.

3.3 Application of the Y-cut resonator to IR detection

The resonance frequency of a Y-cut quartz resonator is sensitive to temperature. This sensitivity has been exploited in thermometers made of single, macroscopic quartz resonators which can accurately detect temperature changes of microkelvins[1]. It has been theoretically shown[2] that a microresonator can be a high performance **IR** sensor because of its high temperature sensitivity and the intrinsic low noise characteristics of quartz crystal oscillators

3.3.1Principle of Operation

The incident radiation from the Infrared source that is absorbed on the sensor (the Y-cut Quartz Resonator) creates a change in the temperature of the material. This change in temperature of the sensor causes a shift in the resonance frequency of the quartz resonator.

3.3.2 Detectivity of the Quartz resonator

The detectivity of the resonator depends on the noise level of the resonator in ambient atmosphere. The noise in the fabricated resonator can be shown as (Figure **3-10**)

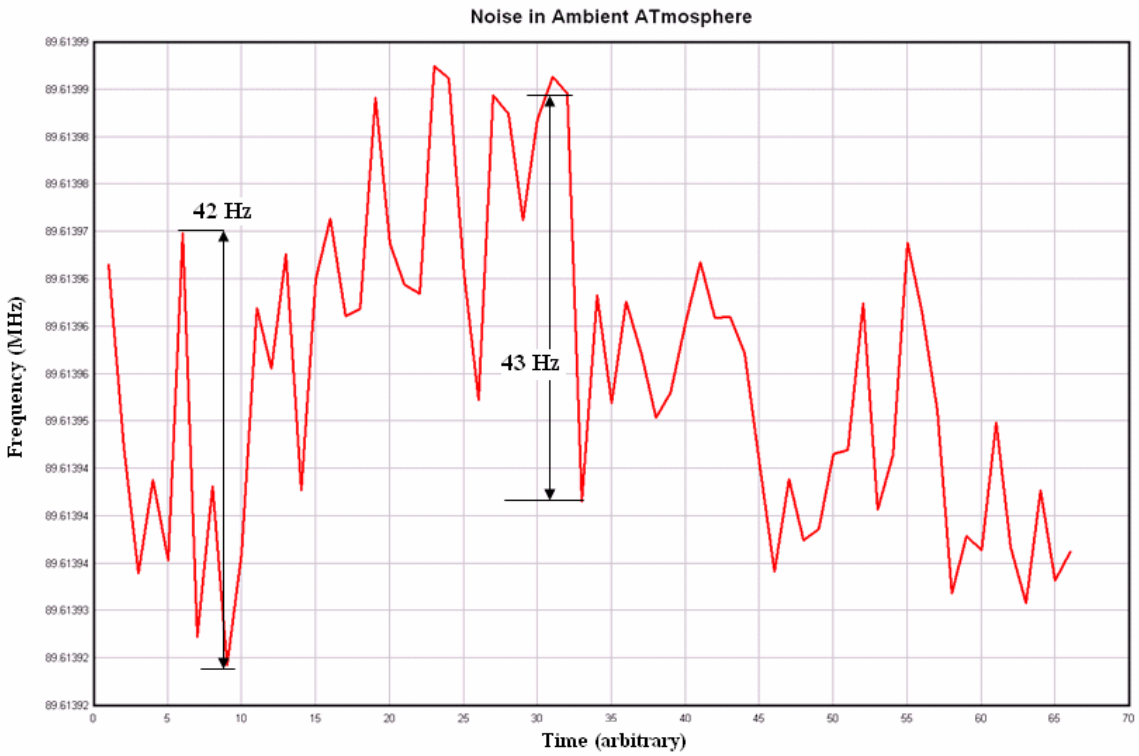

Figure 3-10: Noise levels in Ambient air for the Y-cut resonator.

As seen from the above chart, the maximum noise is about 45 Hz. The calculated RMS (root mean square) noise is 24.5 MHz. It should be possible for us to detect a frequency shift of twice the noise using the sensor i.e. ~50 Hz.

3.3.3 Measurement Setup

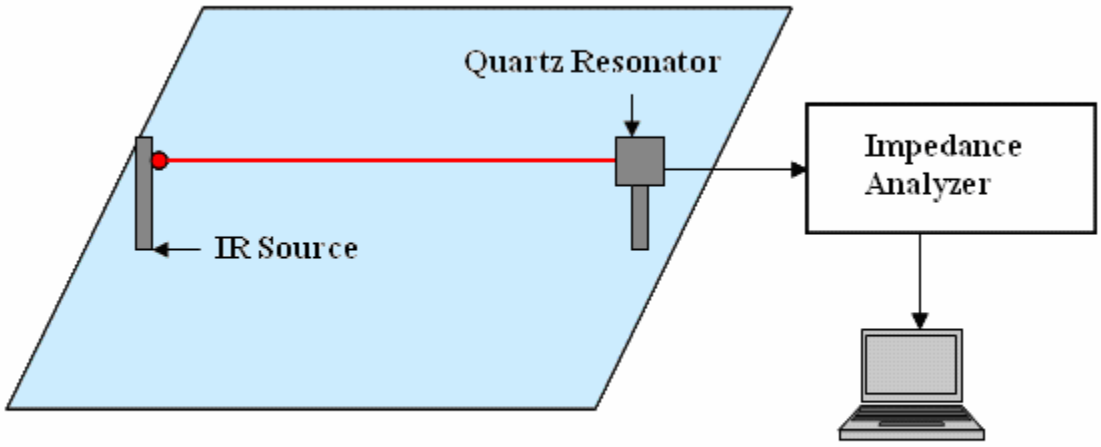

Figure 3-11: Measurement setup for IR sensing

In order to quantify the IR measurement capability of the Y-cut quartz resonators, a measurement setup was made as shown in Figure 3-11 . A collimated Pulsed Infrared Radiator obtained from Ion Optics Inc. to be used as an IR source. This source gives a high intensity beam of IR radiation along a narrow optical path. The micro machined quartz resonator is placed in front of it such that the IR beam falls on the resonator. The IR source is driven by a square wave constant voltage waveform. This produces a pulsed IR radiation and the response of the sensor to the radiation can be measured. The change in frequency of the resonator is measured using an impedance analyzer and the data is acquired, using a LabVIEW program. The total heat delivered by the IR source was measured using a Heimann HTS series sensor

3.3.4 Response of the Resonator

The heat radiated by the IR source was measured using the Heimann sensor with a sensitivity of 29.5 V/W. The Heimann sensor was connected in place of the resonator shown in Figure **3-11** and the voltage response was measured by a voltmeter. The total response was 2.25 mV which gives a total of 76.27 μW of power incident on the sensor.

Since this power is incident on the total sensor area, the power density is given by the ratio of the total power to the element (1.2mm square – as given by the manufacturer) area and can be shown as:

$$Power\,Density\,(Q) = \frac{Total\,Power}{Area} = \frac{7.627 \times 10^{-5}}{\left(1.2 \times 10^{-3}\right)^2} = 52.966\,\frac{W}{m^2} \qquad \textbf{3.6}$$

The temperature profile of the *Y*-cut quartz resonator can be modeled as a circular membrane of radius "a" and uniform thickness "d". The electroded area is smaller than the pixel area and can be considered as a circle with a radius "r" where, r<a. The radial temperature profile of the quartz membrane can be modeled by the two dimensional heat conduction equations, if one ignores the heat losses (radiation and convection) and assume uniform heat generation '*Q'* per unit time per unit area over the whole pixel area.

If the boundaries of the circular quartz membrane are clamped at ambient temperature, the solution of the heat conduction equation can be written as [3]

$$\Delta T(r)\,|_{Membrane} = \frac{Q\left(a^2 - r^2\right)}{4k_{\|}\,d} \qquad \textbf{7.3}$$

Where,

$\Delta T(r)$ is the temperature difference between the pixel membrane at radius *r* and the rim of the membrane (radius a)

$k_{\|}$ is the planar thermal conductivity of the membrane = $1.38\,\frac{W}{mK}$ for Y-cut quartz.

The average temperature for the electroded area ie: radius a/2 can be given as[4]

$$\Delta T(r)\,|_{Avg} = \frac{11Qa^2}{48\,k_{\|}\,d} \qquad \textbf{3.8}$$

Substituting the constants, we get

$$\Delta T(r)\,|_{Avg} = 2.244\times10^{-3}\,Q \qquad \textbf{3.9}$$

But from Eq. **3.6** we know that the total power density incident is 52.966 W/m^2. Substituting, we get

$$\Delta T(r)\,|_{Avg} = 0.1188^{o}\,C \qquad \textbf{3.10}$$

These measurements were made on Device D which has a sensitivity of 7161.18Hz/^{o}C (Figure **3-94**).Hence we should get a total frequency shift (theoretical) of Eq. **3.11** if the entire energy incident is absorbed by the resonator.

$$\Delta f = 0.1188 \times 7161.18 = 850.74\,Hz \qquad \textbf{3.11}$$

However the shift that is observed is as shown in Figure **3-12**

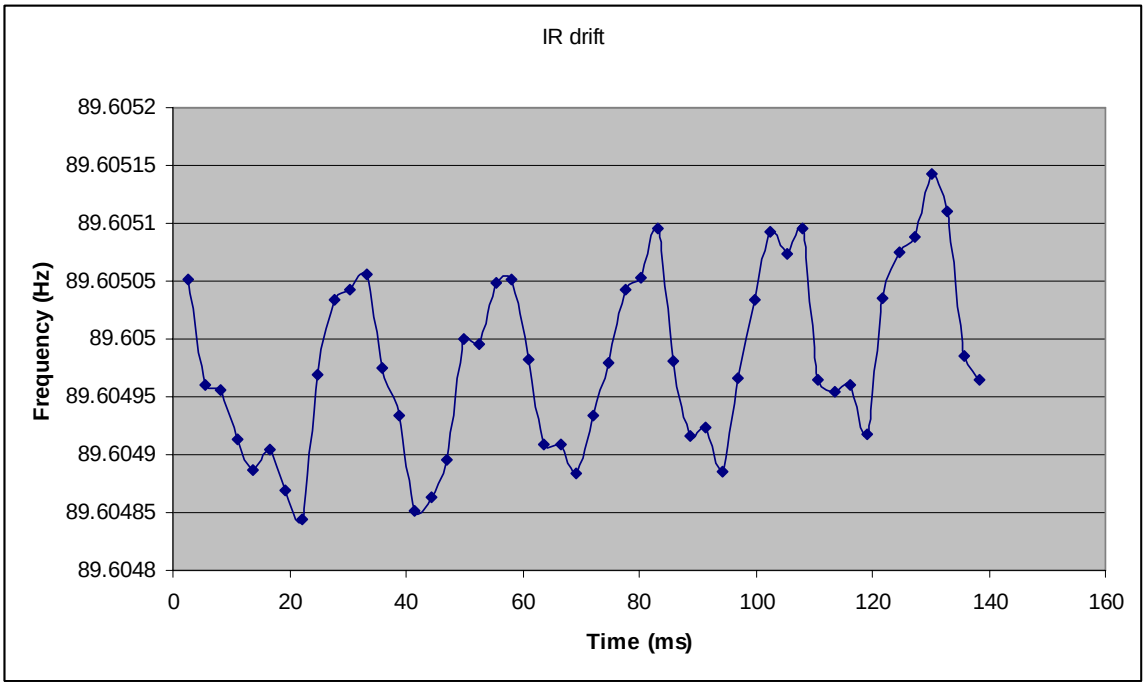

Figure **3-12**: Frequency Shift in the Y-cut resonator in response to infrared radiation

The frequency change seen for every pulse of IR radiation is about 220 Hz. This can be explained because, the surface of the resonator is covered by gold (10 nm) and all the incident radiation is not absorbed. If 50% [**1**] of the radiation is absorbed, then we expect to get a shift of about 425 Hz. The smaller shift is can be explained by the

reflectivity of gold and the loss of heat to the surroundings and the measurement setup. It is possible to improve the absorptivity of the sensor by coating it with various films [2] such as Ti [1].

3.3.5 Effect of ambient temperature shift on the resonator.

The resonator was used to measure the Infrared signal in ambient air. The resonator followed the shift in the ambient temperature as a drift superimposed over the frequency drift due to the IR radiation. As can be seen in Figure **3-13** , this drift can be removed to give the actual signal. In order to ensure that the entire observed shift in frequency is due to the heat source (in this case IR radiation) to be measured, it is necessary to keep the sensor in a temperature controlled environment.

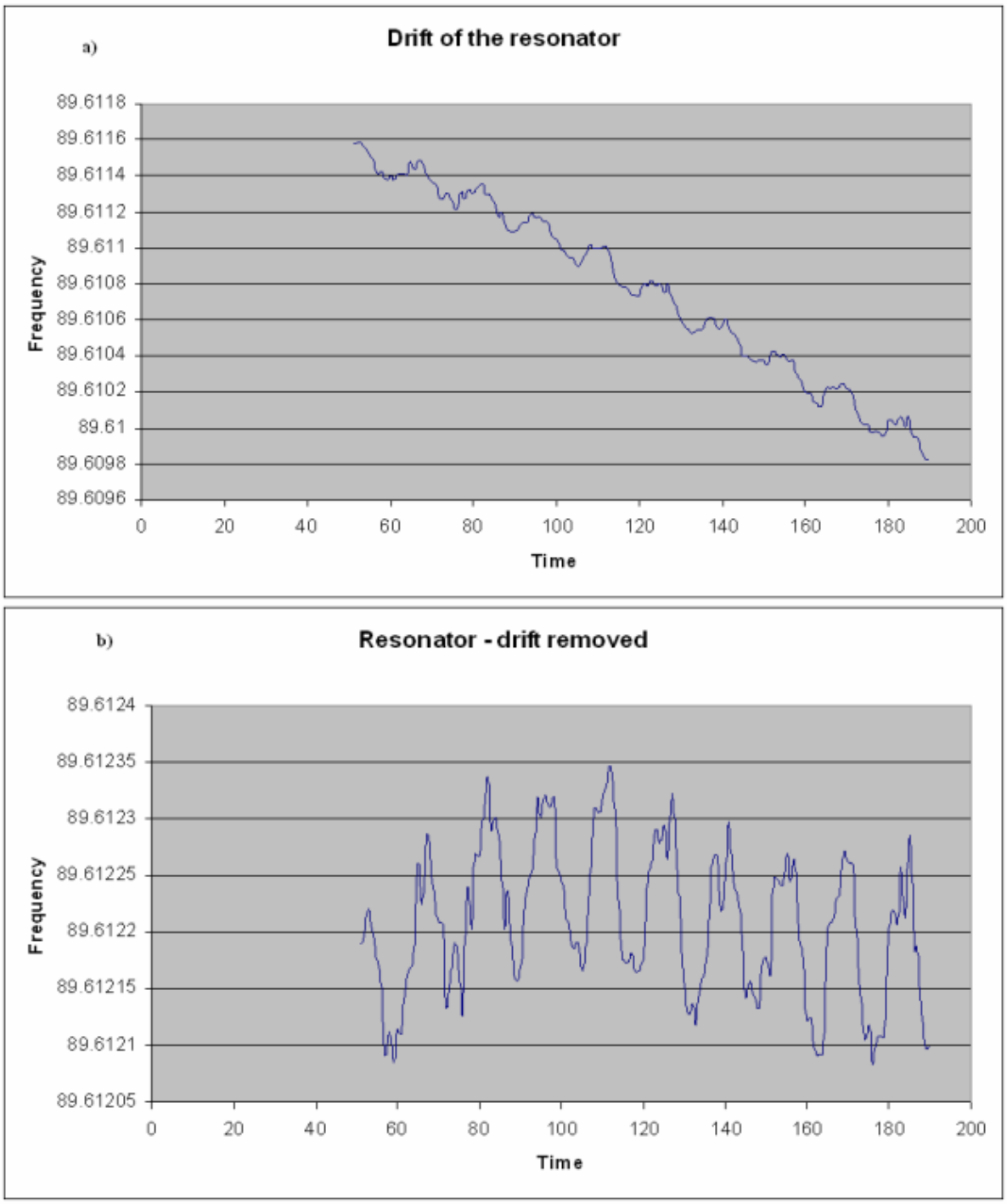

Figure 3-13: a) Measurement of the signal in the presence of Ambient Drift
b) The signal as seen when the drift is removed

Another method to minimize the temperature drift is to carry out a differential measurement on two pixels simultaneously. The infrared emission can be incident on one resonator pixel and the other pixel can be protected from the incident radiation. The drift in the frequency of the second resonator pixel would only be due to the temperature drift in the ambient atmosphere. Subtracting this drift from the drift of the resonator that has been exposed to IR radiation will give us the net shift only attributed to the infrared signal. This method will be discussed in the next Chapter.

1. Yoonkee Kim and John R Vig "*Experimental Results on a Quartz Microresonator IR Sensor*" 1997 IEEE Symposium

2. John R. Vig, Raymond L. Filler and Yoonkee Kim "*Microresonator Sensor Arrays*" 1995 IEEE International Frequency Control Symposium.

3 Carslaw, H.S., and J.C. Jaeger, "*Conduction of Heat in Solids"*. 1959,Oxford: Oxford University Press

4 Abhijat Goyal, Yuyan Zhang, and Srinivas Tadigadapa "*Y-cut Quartz Resonator based Calorimetric Sensor*" IEEE Sensors 2005.

5. J.F. Rosenbaum "*Bulk Acoustic Wave Theory and Devices"* Artech, Boston, 1988.

6. Janshoff, A., H.J. Galla, and C. Steinem, "*Piezoelectric mass-sensing devices as biosensors - An alternative to optical biosensors?"* Angewandte Chemie-International Edition, 2000. **39**(22): p. 4004-4032

Conclusions and Future Work

4.1: Conclusions

A process for the fabrication of micro machined quartz resonators has been designed and perfected. Resonators with a fundamental frequency of up to 90 MHz (~18 μm thickness) have been successfully fabricated. Device characteristics were analyzed and compared to theory. A calibration of the temperature sensitivity of the quartz resonators at room temperature was done. The resonator was used as a thermal Infrared detector.

4.2: Future Work

We have concentrated on the application of the Y-cut resonator as a thermal sensor due to its high temperature sensitivity (90ppm/^{o}C). However this sensor is also sensitive to the mass adhered to its surface. One of the applications proposed for the fabricated resonator is to use it as a thermal biosensor. For example an exothermic reaction based on a catalytic reaction can be used for the design of such a sensor. Specifically reactions such as the catalytic reduction of glucose by glucose-oxidase (-80 kJ/mol), urea by urease (-60 kJ/mol) or hydrogen peroxide by catalase (-87.55kJ/mol) can be readily detected using such a sensor. To do the experiment it is proposed that a known quantity of sugar solution be dropped on the resonator pixel and be allowed to stabilize.

Glucose-oxidase will then be added and the resulting increase in temperature due to the exothermic reaction can be recorded using the resonators. The shift in the frequency will be directly related to the amount of glucose present in the analyte solution

4.2.1: Development of an Oscillator Circuit to monitor the Resonance Frequency of the Quartz Resonators

In order to monitor the frequency shift of the quartz resonator with temperature in real time, the development of an oscillator circuit is proposed. The proposed circuit will oscillate at the frequency determined by the resonator in real time. The real time monitoring of the frequency has the advantage of being able to monitor fast enzymatic reactions and the frequency shift can be calibrated to give the temperature change.

Crystal controlled oscillators are built using an amplifier and a feedback network that selects a part of the amplifier output and returns it to the amplifier input. A generalized depiction of such a circuit can be as shown in Figure 2-1

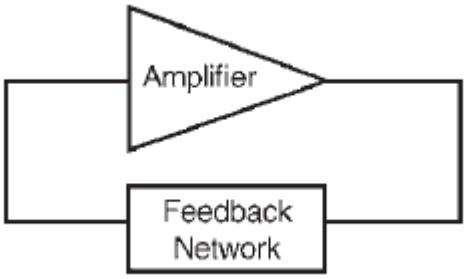

Figure 2-1 Generalized Oscillator Circuit

In order for the circuit to oscillate, two basic criteria must be met

1) The feedback must be positive
2) The Barkhausen criteria must be met [1][2]: ie: The loop power gain must be equal to or greater than unity, and the phase shift must be a multiple of 2π.

Once both these conditions are met, the circuit will oscillate.

The frequency at which an oscillator operates is dependent on the loop phase angle shifts within the oscillator circuit. A crystal oscillator can be used in the feeback loop to provide a stable frequency of oscillation.

In a crystal oscillator, the impedance of the quartz crystal changes so dramatically with changes in the applied frequency that all other circuit components can be considered as being of essentially constant reactance. Therefore, when a quartz crystal is used in the feedback loop of an oscillator, the frequency of the oscillator circuit will adjust itself so that it presents a reactance which satisfies the loop phase requirements. A depiction of the reactance vs. frequency of a quartz crystal unit is as shown below in Figure 2-2

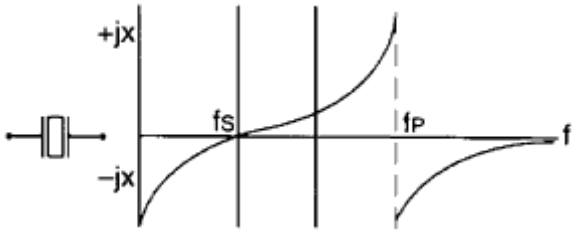

Figure 2-2: Reactance v/s Frequency for the QCM [10]

As one can see from the above figure, a quartz crystal unit has two frequencies of zero phase. The first, or lower of the two, is the series resonant frequency (*f*). The second, or

higher of the two frequencies of zero phase is the parallel, or anti-resonant frequency (parallel resonance frequency), f_p. The series resonant frequency appears resistive in an oscillator circuit. At the series resonant point, the impedance is minimum and the current flow is maximum since the reactance is zero. The series resonance frequency can be given as:

$$f_s = \frac{1}{\sqrt{2\pi L1 C1}}$$

As the frequency is increased beyond the point of series resonance, the crystal appears inductive in the circuit. When the reactance of the motional inductance and shunt capacitance cancel, the crystal is at the frequency called Anti-resonance Frequency (f_p). At this point, the impedance is largest in the circuit and the current flow is minimum. The frequency of a crystal at f_p is inherently unstable and is never selected as the frequency of operation for an oscillator. The parallel resonance frequency is given as:

$$f_p = \frac{f_s}{\sqrt{1 + \frac{C1}{C0}}}$$

The region between f_s and f_p is typically called "Area of Parallel Resonance". Parallel resonance can occur by adding load capacitance to the crystal in series resulting in a positive frequency shift determined by:

$$\Delta f = \frac{f_s C1}{2\,(C0 + C1)}$$

Just as there are two frequencies of zero phase associated with a QCM, there are two primary oscillator circuits. These circuits are described by the type of crystal unit to be used, namely “series” or “parallel.”[3]

A series resonant oscillator circuit uses a crystal which is designed to operate at its natural series resonant frequency. In such a circuit, there will be no capacitors in the feedback loop. Series resonant oscillator circuits are used primarily because of their minimal component count. These circuits may, however, provide feedback paths other than through the crystal unit. Therefore, in the event of crystal failure, such a circuit may continue to oscillate at some arbitrary frequency. A standard series resonant oscillator circuit is shown in Figure 2-3

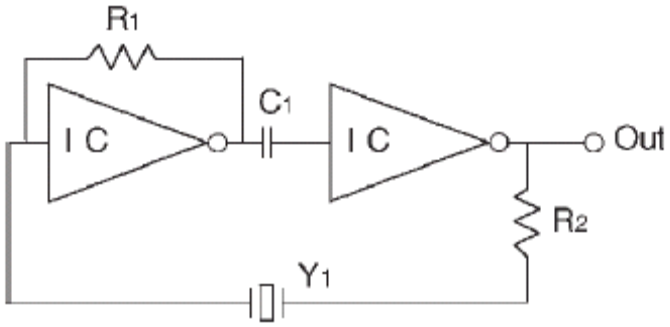

Figure 2-3: Series Resonator Circuit

In the above circuit, resistor R1 is used to bias the inverter and to cause it to operate in its linear region. This resistor also provides negative feedback to the inverter. *Capacitor C1* is a coupling capacitor, used to block DC voltage. *Resistor R2* is used to bias the crystal unit. This resistor also strongly influences the drive current seen by the

crystal unit *Crystal unit Y1* is a series resonant crystal unit, specified to operate at the desired frequency and with the desired frequency tolerance and stability.

A parallel resonant oscillator circuit uses a crystal unit which is designed to operate with a specified value of load capacitance. This will result in a crystal frequency which is higher than the series resonant frequency but lower than the true parallel resonant frequency. These circuits do not provide paths other than through the crystal unit to complete the feedback loop. In the event of crystal unit failure, the circuit will not continue to oscillate. A standard parallel resonance circuit is shown below in Figure **2-4**

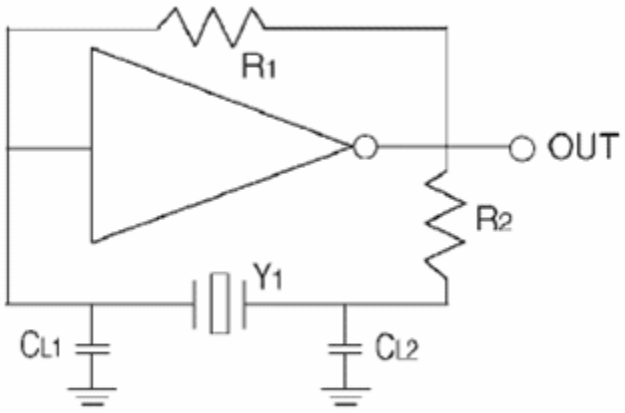

Figure **2-4**: Parallel Oscillator Circuit

This circuit uses a single inverter, with two capacitors in the feedback loop. These capacitors comprise the “load capacitance” and together with the crystal unit, establish the frequency at which the oscillator will operate. As the value of the load capacitance is changed, so is the output frequency of the oscillator. Therefore, this circuit does provide a convenient means of adjusting the output frequency, if any adjustment is required. The resistors R1 and R2 bias the inverter to provide the maximum voltage swing. The two

load capacitors, C_{L1} and C_{L2}, serve to establish the frequency at which the crystal unit and therefore the oscillator will operate. Crystal unit Y1 is a parallel resonant crystal unit, specified to operate with a specified value of load capacitance, at the desired frequency and with the desired frequency tolerance and stability.

4.2.1.1: Proposed Circuit for the fabricated Quartz Resonators

Since our fabricate resonators resonate at about 90 MHZ a high-speed logic circuit was necessary to sustain oscillations. A CMOS inverter circuit [**11**] was simulated for a 90 MHz resonator. This circuit is as shown in Figure **2-5** below. The circuit is based upon a high speed tiny logic inverter with maximum switching frequency of 0.25 GHz(switching speed: 4 ns) from Fairchild semiconductors (NC7s04).

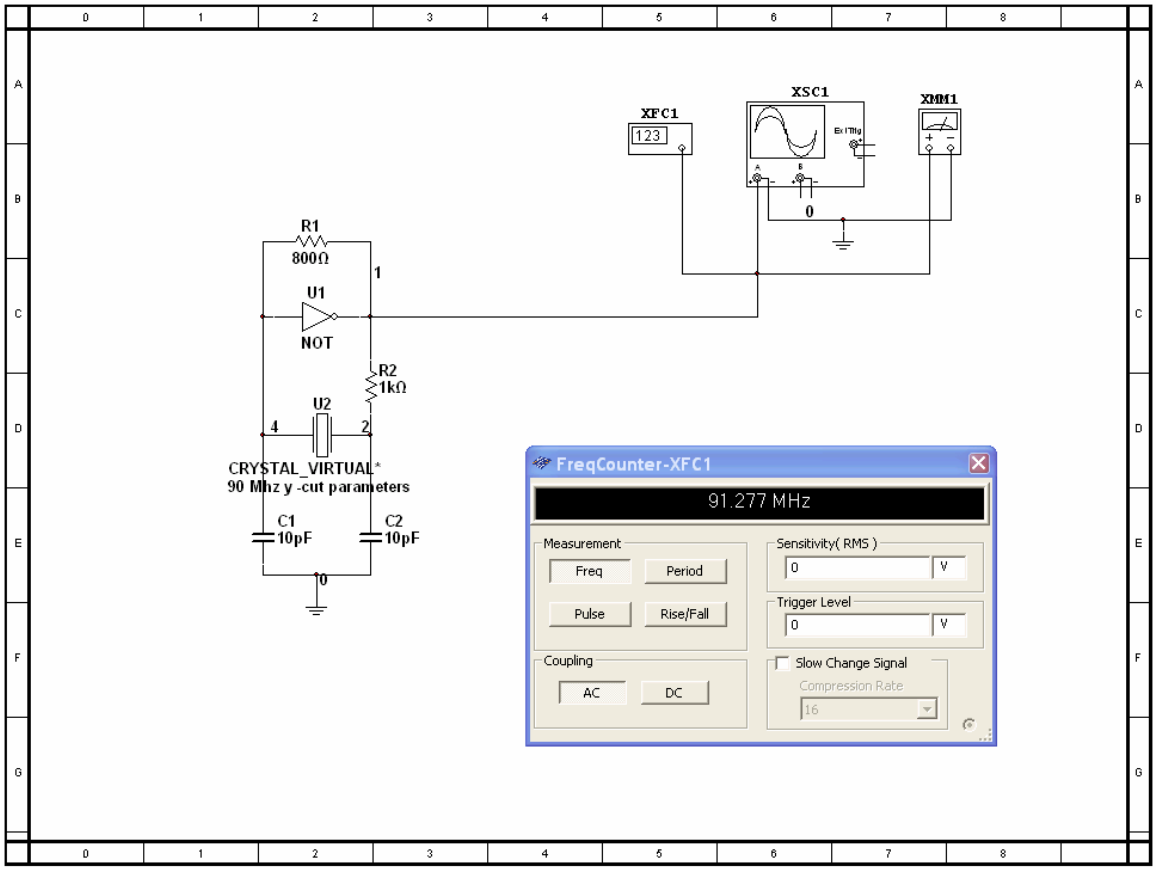

Figure 2-5: CMOS Inverter based Oscillator Circuit

For the above circuit, the crystal parameters were input to be the same as one of the fabricated resonators. The Multisim® simulation of the circuit shows that the oscillator resonates with the frequency determined by the crystal. Such a circuit can be used for the real time monitoring of the QCM to reflect any change in the temperature.

4.2.2: Immobilization of Enzyme on the Electrode of the Quartz Resonator

To be sure that the heat released in an enzymatic reaction, for example, is restricted to a particular pixel, it is proposed to immobilize the enzyme on the top electrode of the fabricated array of individual resonators and then add the glucose solution. This should restrict the heat produced to individual pixels, causing all the heat released in the reaction to influence the frequency change in that specific resonator. This should allow us to maximize the signal for a given amount of analyte concentration and therefore a more accurate estimate of its concentration.

4.2.3: Differential Measurement using Two Pixels Simultaneously:

As mentioned earlier Y-cut quartz resonators are not only sensitive to temperature but are also sensitive to the mass/viscosity of the liquid in contact with its surface. Therefore, the addition of the analyte solution during an enzymatic reaction also results in viscous loading on the resonator. This viscous loading will cause the frequency of the resonator to shift irrespective of the temperature effect. This makes it necessary to separate the two effects: (i) that of the frequency decrease due to mass/viscous loading from the QCM and (ii) the frequency increase caused by the heat released during the enzymatic reaction. In order to separate the two phenomena, it is proposed that simultaneous measurement be made on two pixels, one to compensate for mass loading,

i.e., with no immobilized enzyme but functionalized in an identical way as the active pixel and the second (active pixel) functionalized with the required enzyme. The difference in the frequency shift of the two resonators upon the addition of the identical analyte solution on both pixels will accurately reflect the temperature signal arising due to the exothermic enzymatic reaction and can then be used to determine the analyte concentration. The circuit proposed in section 4.2.1 can be used for such monitoring.

1. Robert L. Boylestad and Louis Nashelsky "Electronic Devices and Circuit Theory" 7th edition 1999

2. Donald A Neamen "Electronic Circuit Analysis and Design" 2nd edition

3. FOXElectronics: "Oscillator –Theory of Operation"

4. http://www.4timing.com/techcrystal.htm

5. Rudolf F Graf KA2CWL "Crystal Oscillators and Circuits"

6. Jun MATSUOKA, Tomio SATO, and Tsuyoshi OHSHIMA "A Circuit for High Frequency Crystal Oscillators" Proceedings of the 2003 IEEE International Frequency Control Symposium and PDA Exhibition Jointly with the 17th European Frequency and Time Forum

7. Application Note: Texas Instruments 'Use of the CMOS Unbuffered Inverter in Oscillator Circuits'

8. Jelena PopoviC, Aleksandra Pavasovie, Zdenka ZivkoviC-DZunja, and Dragan VasiljeviC "CMOS RLC and Crystal Oscillators Based on Current Conveyors" IEEE TRANSACTIONS ON ULTRASONICS, FERROELECTRICS, AND FREQUENCY CONTROL, VOL. 43, NO. 3, MAY 1996

9. Fairchild Semiconductor: Application Note: "HCMOS Crystal Oscillators"

10. Fortiming "*Basic Technology of Quartz Crystal Resonators*

11. Horrowitz and Hill "The Art of Electronics" Cambridge University Press 1980

Appendix A

Mathematica Program used to split the data file from the Impedence Analyser Agilent 4294A

```
Data=Import["C:\\Documents and Settings\\Ashish\\My
Documents\\Thesis\\expts\\y cut cali\\4-60.dat","TSV"];
NoOfDataPoints=602;
FileName="a"<>ToString[#]<>".dat"&/@Range[Length[Data]/NoOfD
ataPoints];
IndexValues=Partition[Range[Length[Data]],NoOfDataPoints];In
dexValues=Drop[IndexValues,{},{1}];(* I don't remember if
the files should have a .txt extension. If you don't need
the extension then just delete '<>".txt"' after ToString[#]
*)
     ExportPath="C:\\Documents and Settings\\Ashish\\My

Documents\\Thesis\\expts\\y cut cali\\4-60\\";(*Export path

is the path of the folder you would like to export the files

to

*)Export[ExportPath<>FileName[[#1]],Data[[IndexValues[[#1]],

{1,3}]],"TSV"]&/@Range[Length[FileName]];
```

Appendix B

Mathematica Program to fit the Resonance Curve of the QCM

```
<<Statistics`NonlinearFit`          (*Loads the non-linear
fitting package*)
SetDirectory["C:\\Documents and Settings\\aap196\\My
Documents\\QCMsoftware\\Folder602\\"]    (*Sets the data
directory*)

fitfn=a0+A*((f/fo)*Cos[phi]+(1-(f/fo)^2)* Q*
Sin[phi])/((f/fo)^2+(1-(f/fo)^2)^2*Q^2)(*Defines the fitting
function*)

datfiles=FileNames["a*.dat"];(*Defines a list of data files
to fit,performs the fit on each of the data files.Reports
time required, fitted parameter values (fo and Q),and fit
statistics.Results are written to a text file.*)

paraml={};     (*defines an arbitary parameter for output of
the results*)
Do[Print[datfiles[[j]] "working on:"];
data=Drop[ReadList[datfiles[[j]],Real,RecordLists→True(*m
akes sure that the data is arranged in pairs rather than a
single column vector*)],1(*this causes the first element to
be dropped from the list*)];(*the statement do ends here*)
(*makes a list of data in pairs of two, the freqeuncy and
the corresponding amplitude*)
  ImpdMax=Max[data[[All,2]]];
  ImpdMin=Min[data[[All,2]]];
  Aest=ImpdMax-ImpdMin;
  f0est=data[[Position[  data[[All,2]],ImpdMax
]][[1,1]],1]];
  Print[ImpdMax];
  Print[ImpdMin];
  Print[Aest];
  Print[f0est];
  peakfit=Timing[{BestFit,BestFitParameters,ANOVATable}
/.NonlinearRegress[data,fitfn,f,{{a0,ImpdMin},{fo,f0est},{ph
i,1},{Q,7500},{A,Aest}},RegressionReport→{BestFit,BestFitPa
rameters,ANOVATable}]];

Export[StringJoin[ToString[datfiles[[j]]],".mprm"],peakfi
t[[2,2]],"Table"];

datafit=Show[{Plot[peakfit[[2,1]],{f,data[[1,1]],Last[data][
[1]]},PlotStyle→RGBColor[1,0,0],DisplayFunction→Identity],L
```

```
istPlot[data[[All,{1,2}]],Prolog→AbsolutePointSize[1],Displ
ayFunction→Identity,PlotJoined→True]},GridLines→None,PlotRa
nge→All,PlotLabel→ToString[datfiles[[j]]],Axes→False,Prol
og→AbsolutePointSize[0.2],DisplayFunction→$DisplayFunction]
;
  Print[peakfit[[1,1]] "Seconds Required"];
  Print[NumberForm[peakfit[[2,2,2]],15]];
  Print[peakfit[[2,2,4]]];
  Print[peakfit[[2]]];

paraml=Append[paraml,{datfiles[[j]],NumberForm[fo/10^6,15]/.
peakfit[[2,2,2]],NumberForm[Abs[Q],5]/.peakfit[[2,2,4]]};,{
j,1,Length[datfiles]}];
Export["mdata.txt",paraml,"Table"];
Export["freqs.dat",paraml,"Table"];
     Print[TableForm[paraml]]
```